J. Fluid Mech. (1996), *vol.* 309, *pp.* 45–84

Wall-vorticity flux dynamics in a two-dimensional turbulent boundary layer

By J. ANDREOPOULOS AND J. H. AGUI

Experimental Fluid Mechanics and Aerodynamics Laboratory, Department of Mechanical Engineering, The City College of the City University of New York, Convent Av. and 140th Street, New York, NY 10031, USA

(Received 13 April 1994 and in revised form 26 June 1995)

Four high-frequency-response pressure transducers with 10 viscous units resolution each have been used to obtain simultaneously the fluctuating pressure gradients at the wall of a zero-pressure-gradient boundary layer and then to compute the vorticity flux away from the wall. Since the viscous force on an element of incompressible fluid is determined by the local vorticity gradients, understanding of their dynamical characteristics is essential in identifying the turbulent structure. Extremely high and low amplitudes of both vorticity gradients have been observed which contribute significantly to their statistics although they have low probability of appearance. The r.m.s. of the vorticity flux when scaled with inner wall variables depends very strongly on the Reynolds number, indicating a breakdown of this type of scaling. The application of a small threshold to the data indicated two preferential directions of the vorticity flux vector. An attempt has been made to identify these high- and low-amplitude signals with physical phenomena associated with bursting–sweep processes. Vortical structures carrying bipolar vorticity are the dominant wall structures which are associated with the violent events characterized by large fluctuations of vorticity flux.

1. Introduction

The role of vorticity, defined as the curl of the velocity vector, in better understanding various fluid dynamics phenomena, is well established. Lighthill (1963) in his wide-ranging introduction to boundary-layer theory, provided an extensive description of vorticity dynamics in a variety of flows by using vorticity as a primative variable for theoretical considerations. He was also the first to introduce the concept of 'vorticity flux' density and to point out the significance of solid boundaries as distributed sources or sinks of vorticity. Vorticity production at a solid boundary can be described in terms of vorticity flux. Lighthill (1963) defined the term for two-dimensional flows by analogy to Fourier's heat conduction law as

$$-\nu\left(\frac{\partial\omega}{\partial y}\right)_w, \tag{1}$$

where ω is the vorticity vector and ν the viscosity, and Panton (1984) extended this approach to include three-dimensional flows by defining vorticity flux as

$$\sigma = -\nu(\boldsymbol{n}\cdot\nabla\omega)_w, \tag{2}$$

where $\boldsymbol{n}$ is the normal vector to the surface, towards the fluid (see figure 1 for the coordinate system).

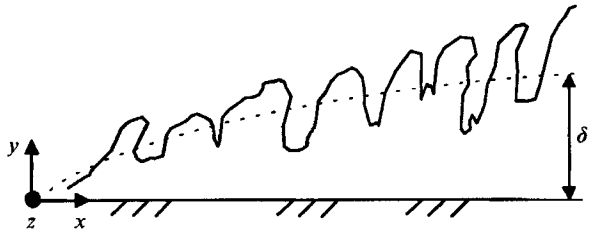

FIGURE 1. Boundary-layer flow schematic and coordinate system.

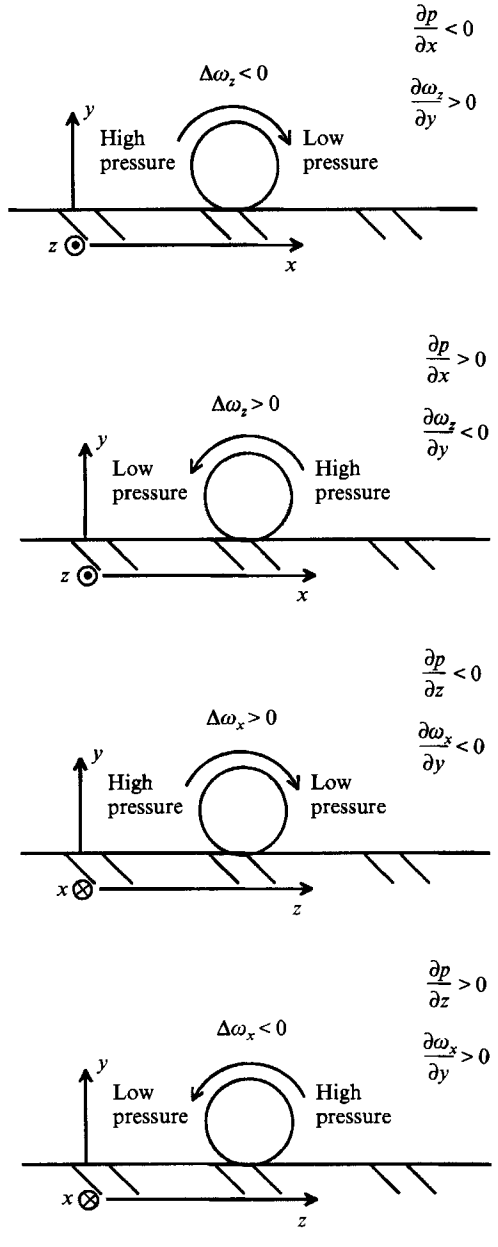

FIGURE 2. Lighthill's (1963) mechanism of vorticity acquisition of an initially irrotational fluid element.

Lyman (1990) pointed out that the analogy to Fourier's law may not be exact in three-dimensional flows. He proposed an alternative definition of vorticity flux as

$$\nu \boldsymbol{n} \times (\nabla \times \boldsymbol{\omega}). \tag{3}$$

Although both definitions (2) and (3) express the rate of vorticity production per unit area of surface, they are not equivalent. This is easily seen by examining their components at a solid surface. When integrated over a closed control surface, however, both definitions give the same result because as shown by Lyman (1990) and Panton (1984)

$$-\iint_S \nu(\boldsymbol{n}\cdot\nabla\boldsymbol{\omega})\,\mathrm{d}S = \iint_S \nu \boldsymbol{n}\times(\nabla\times\boldsymbol{\omega})\,\mathrm{d}S = \iiint_V \nu\nabla^2\boldsymbol{\omega}\,\mathrm{d}V, \tag{4}$$

where the last integral represents the result of integrating the viscous diffusion term in the vorticity transport equation while the other two surface integrals are identified as the result of integrating the vorticity flux.

Lighthill has also pointed out that vorticity flux is directly related to pressure gradient at the wall, although the transport equation of vorticity contains no pressure. If the momentum equation is evaluated at the wall beneath a turbulent flow it yields

$$\left[\frac{1}{\rho}\frac{\partial p}{\partial x}\right]_w = -\left[\nu\frac{\partial \omega_z}{\partial y}\right]_w, \tag{5}$$

$$\left[\frac{1}{\rho}\frac{\partial p}{\partial z}\right]_w = \left[\nu\frac{\partial \omega_x}{\partial y}\right]_w, \tag{6}$$

where p is the pressure and ω_x, ω_z are the longitudinal and transverse vorticity components. Figure 2 shows how Lighthill has depicted the mechanism of vorticity acquisition of an initially irrotational small fluid ball at the wall beneath a flow: a pressure gradient tangential to the boundary causes the fluid ball to roll along a stationary wall due to the non-slip condition at the wall.

In the present work the following definition has been adopted for the vorticity flux, at a stationary wall beneath viscous flows:

$$\boldsymbol{\sigma}_w = -\nu\left[\frac{\partial \omega_x}{\partial y}\right]_w \boldsymbol{i} - \nu\left[\frac{\partial \omega_z}{\partial y}\right]_w \boldsymbol{k}, \tag{7}$$

where $\boldsymbol{i}, \boldsymbol{j}, \boldsymbol{k}$ are unit vectors in the x-, y- and z-directions respectively. This definition, which in fact is Lyman's suggestion, enables one to measure directly vorticity flux at the wall by measuring the pressure gradients along the wall.

None of the above equations are time-averaged relations and therefore they can provide time-dependent information on the vorticity flux entering the flow which cannot be obtained by considering vorticity at the wall. This value is related to the wall shear stress $\boldsymbol{\tau}_w$ through

$$\boldsymbol{\omega}_w \times \boldsymbol{n} = \frac{\boldsymbol{\tau}_w}{\mu}, \tag{8a}$$

where $\boldsymbol{\omega}_w$ is the vorticity vector at the wall. For two-dimensional flows and after time averaging, (8a) becomes

$$\bar{\omega}_z = \frac{\bar{\tau}_{yx}}{\mu}. \tag{8b}$$

This relation indicates that when the skin friction is known, the value of ω_z at the wall can be found.

If the pressure gradients $\partial p/\partial x$ and $\partial p/\partial y$ can be measured instantaneously, the vorticity flux away from the wall can be computed through (5), (6) and (7) as a time-

dependent function. Then the vorticity change shed from the solid boundary and sensed at a nearby point inside the flow at a distance Δy from the wall, to a first-order approximation, will be

$$\Delta\omega_z = -\left[\frac{\partial\omega_z}{\partial y}\right]_w \Delta y, \tag{9}$$

and

$$\Delta\omega_x = -\left[\frac{\partial\omega_x}{\partial y}\right]_w \Delta y. \tag{10}$$

Since $\Delta y > 0$ always, the signs of $\partial p/\partial x$ and $\partial p/\partial y$ determine whether the wall acts as a source or sink of vorticity.

Time-resolved measurements of the wall pressure fluctuations, or wall shear stress or wall velocity gradient have the potential of revealing significant information on the wall turbulence structure. Johansson, Her & Haritonidis (1987), Thomas & Bull (1983), Haritonidis, Gresko & Breuer (1988), for instance, measured wall pressure fluctuations and shear stress which revealed a strong coupling between wall pressure and flow structures near the wall, while Hanratty (1988) demonstrated the existence of a flow pattern containing a large number of counter-rotating eddies. Although the structure of the near-wall turbulence has been extensively investigated over the past thirty years, the basic mechanism for turbulence production and transport is not well understood. Mutual interactions between various structures present in the near-wall region and between inner- and outer-layer flow complicate the understanding of turbulence structure. Despite this lack of understanding it is well documented that in the vicinity of the wall, the flow has been found to be highly organized, consisting of regions of high- and low-speed fluid alternating in the spanwise direction (Kline *et al.* 1967). The existence of streamwise vortices and shear layers emanating from the wall have also been observed experimentally by Blackwelder & Eckelman (1979) and Johansson *et al.* (1987). Several of the structures found to exist in near-wall turbulence have also been observed in direct numerical simulations (Moin & Kim 1985; Jimenez & Moin 1991; Kim 1989).

The objective of the present investigation is to increase our understanding of the vorticity dynamics in the region very near to the wall of a zero-pressure-gradient, two-dimensional turbulent boundary layer. This has been accomplished by measuring the wall pressure gradient $(\boldsymbol{n}\times\boldsymbol{\nabla}p_w) = (\partial p/\partial z)\boldsymbol{i} - (\partial p/\partial x)\boldsymbol{k}$ as a function of time and subsequently computing the vorticity gradients and vorticity flux away from the wall by using the previously mentioned relations. The paper reports on measurements of vorticity flux obtained at various Reynolds numbers. To our knowledge this type of measurement has not been attempted before.

2. Experimental set-up and instrumentation

The experiments were performed at the CCNY large-scale wind tunnel, which is powered by a 20 b.h.p. frequency-controlled motor which provides 40000 c.f.m. of air at a maximum free-stream velocity of approximately 11 m s^{-1}. The rectangular flow inlet is 12 ft by 12 ft and includes a honeycomb and five mesh screens. The test section is 4 ft by 4 ft and 28 ft long. Qualification measurements indicate a 0.08% turbulence intensity in the free stream at maximum velocity and 0.15% at 3 m s^{-1}. To minimize vibration, the working section was isolated from the downstream axial fan and motor. The motor and fan assembly is housed in a sound-absorbing diffuser with porous wall thus allowing low noise operation of the facility and low levels of acoustical noise transmitted in the working section.

Exp	u_e	δ (mm)	δ^*/θ (mm)	Re_θ	C_f	u_τ (m s^{-1})	d^{+*}	Δt^+	$\Delta x^+, \Delta z^+$	$Re^* = \frac{u_\tau \delta^*}{\nu}$	$Re^+ = \frac{u_\tau \delta}{\nu}$
1	5.5	90	11.6/8.9	3100	0.0034	0.228	10	0.333	22	169	1315
2	6.5	87	11.24/8.6	3580	0.0033	0.264	12	0.446	27	190	1472
3	7.15	85	11.18/8.5	3900	0.0032	0.289	13	0.535	42	207	1575
4	8.25	83	10.54/8.2	4350	0.00319	0.329	15	0.693	33	222	1750
5	9.35	81	10.25/8	4800	0.0031	0.368	16.5	0.868	37	241	1910
6	11	76	9.64/7.7	5400	0.00301	0.426	19	1.163	42	263	2075

TABLE 1. Nominal flow parameters of the incoming boundary layers

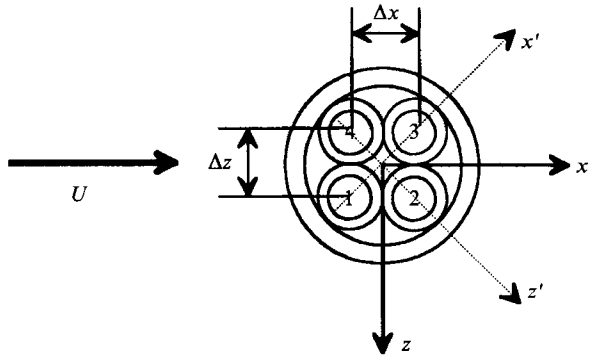

FIGURE 3. Pressure transducer configuration.

The boundary layer is developed on the floor of the wind tunnel and it was tripped by means of a $\frac{1}{2}$ in. wide strip of sandpaper of medium grit glued on the wind tunnel wall at the end of the contraction. All measurements took place at a distance 4 m downstream of the beginning of the working section. Six experiments were run at different Reynolds numbers. Table 1 shows the nominal flow parameters of the incoming boundary layers. The skin-friction coefficient was determined through Clausert chart plots and Preston tube measurements. Four high-frequency-response and high-sensitivity subminiature pressure transducers model XCS-062-5-D, as supplied by Kulite Semiconductor Products, were used to determine the wall pressure gradients $\partial p/\partial x$ and $\partial p/\partial y$ by measuring the time-resolved pressure simultaneously at all transducers. The resonant frequency of these transducers as stated by the manufacturer was 150 KHz. Shock-tube tests, including static and dynamic calibrations, in our laboratory and elsewhere, indicate a frequency response of the transducers close to this value. Considerable attention has been given to the spatial resolution of the transducers in the viscous subrange. Their sensing area was circular with 0.71 mm diameter. Table 1 also indicates the corresponding transducer size d^+, expressed in viscous lengthscales ν/u_τ, of the various experiments. As will be discussed later, the resolution of the present experiments compares quite favourably with that obtained by other investigators. In fact, to the best of our knowledge, the present case of the lowest $Re_\theta = 3150$ represents an experiment with the most resolved scales of pressure fluctuations so far. Schewe (1983) has documented that pressure transducers of diameter $d^+ \approx 20$ are able to resolve pressure signatures significant to the structure of turbulence.

The smallest scale encountered in the flow is of the order of the Kolmogorov lengthscale $\eta = [\nu^3/\epsilon]^{1/4}$ where ϵ is the dissipation rate of the turbulent kinetic energy. Determining η requires a good estimate of ϵ, which is very difficult to measure, particularly at the wall, where it has never been measured. Honkan (1994) has recently measured ϵ above the wall at $y^+ = 12.5$ by using a nine-wire vorticity probe similar to the probe of Balint, Wallace & Vukoslavcevic (1991). His work was carried out in the same wind tunnel facility as the present investigation and under very similar flow conditions. His results agree rather well with the measurements of Balint *et al.* (1991) as well as with those of Klewicki & Falco (1990). If Honkan's estimate of ϵ is extrapolated to the wall and used in the present analysis, the size of the pressure transducers appears to be between $\eta_d = 1.5$ and 2.6.

The pressure transducers were placed close to each other, at a distance of $\Delta x = 1.6$ mm inside the plywood wall of the wind tunnel so that the pressure

transducer surface was flush with the internal wall beneath the flow. Figure 3 shows the configuration of the four transducers that measured time-resolved gradients simultaneously. The following pressure gradients have been computed by using a finite-difference scheme:

$$\frac{\partial p_{21}}{\partial x} \approx \frac{p_2 - p_1}{\Delta x}, \quad \frac{\partial p_{14}}{\partial z} \approx \frac{p_1 - p_4}{\Delta z}, \tag{11}$$

$$\frac{\partial p_{34}}{\partial x} \approx \frac{p_3 - p_4}{\Delta x}, \quad \frac{\partial p_{23}}{\partial z} \approx \frac{p_2 - p_3}{\Delta z}. \tag{12}$$

The distances $\Delta x, \Delta z$ non-dimensionalized by the viscous length of each experiment are also listed in table 1.

In addition to these pressure gradients which are associated with the xoz coordinate system, pressure gradients associated with the $x'oz'$ coordinate system, which is at 45° to the original, are also evaluated by considering the diagonal transducers only:

$$\frac{\partial p_{31}}{\partial x'} \approx \frac{p_3 - p_1}{\Delta x'}, \quad \frac{\partial p_{24}}{\partial z'} \approx \frac{p_2 - p_4}{\Delta z'}. \tag{13}$$

In this case, $\Delta x' = \Delta z' = \sqrt{2}\,\Delta x$. These pressure gradients can be transformed instantaneously back to the original xoz coordinate system by a $-45°$ rotation of the $x'oz'$ system. Thus the results obtained by considering the diagonal transducers only can be used to provide additional estimates of the vorticity flux in the xoz system.

The transducers were calibrated frequently in the calibrator model supplied by Thermo-Systems Inc. Signal conditioning for each analog output of the Kulite transducers was provided by a four EG&G Parc model 113 low-noise differential preamplifiers and four Khon-hite band-pass filters model 3323. Data acquisition was provided by a DAS-20 Metrabyte Analog to Digital Converter daisy chained to a simultaneous sample and hold board all configured on a IBM 386/25 desktop computer. The acquired data were transferred to a DEC 3100 workstation where the major analysis was carried out. The sampling frequency interval expressed in terms of viscous time units ν/u_τ^2 is shown in table 1. To minimize the effect of electronic noise contamination all instruments were powered by batteries and not line power using transformers. The signals were high-pass filtered at 0.01 Hz and low-pass filtered at 5000 Hz. By recording the a.c component of the signal, the signal-to-noise ratio was drastically improved. Acoustical background noise and vibration tests, with or without the flow, indicate a 6:1 signal-to-noise ratio for the lowest $Re_\theta = 3100$ experiment which showed the weakest pressure fluctuations and the worst signal-to-noise ratio of all the investigated cases. An attempt to obtain meaningful data at $Re_\theta = 1900$ failed to produce better than a 2:1 signal-to-noise ratio.

3. Probe resolution

Near-wall measurements are extremely difficult to obtain because the wall imposes tight physical constraints on the required probe measuring volume which determine the measuring position nearest to the wall and the spatial resolution. The problem of spatial resolution of probes is essentially three-dimensional, although the high-velocity gradients in the direction normal to the wall impose more severe requirements on resolution in this direction than in the other two directions. For a probe placed at the wall beneath the flow, however, spatial resolution needs to be considered in two dimensions.

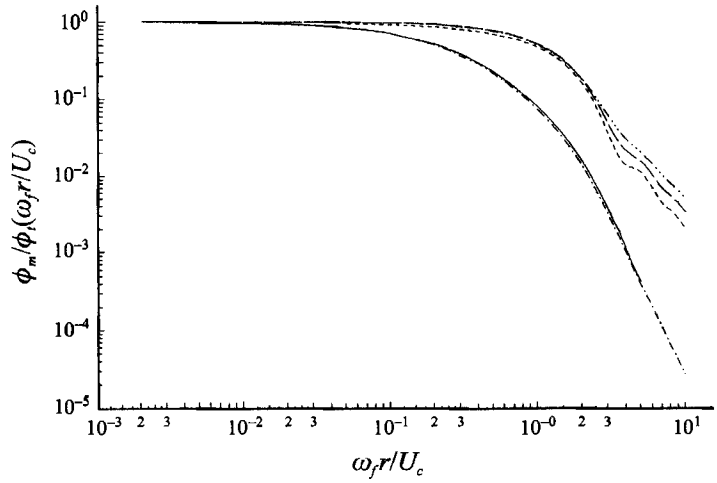

FIGURE 4. Spectral attenuation due to spatial resolution: ----, pressure (Corcos 1963); – – –, pressure (present analysis based on data by Willmarth & Wooldridge 1962); –·–·–·–, pressure (present analysis based on data by Farabee & Casarella 1991); ——, vorticity flux (present analysis based on data by Willmarth & Wooldridge 1962); ·-·-·-·-, vorticity flux (present analysis based on data by Farabee & Casarella 1991).

In order to evaluate the response characteristics of the vorticity-flux probe to turbulent flows with scales smaller than its size, an extension of the theories of Corcos (1963) and Willmarth & Roos (1965) on resolution of pressure measurement has been attempted. The present analysis, which is carried out under the same basic assumptions as the work of Corcos, is described in detail in the Appendix. Typical results of this analysis are shown in figure 4 where the attenuation of power spectral densities of vorticity flux and pressure fluctuations are plotted. Here ϕ_m and ϕ_t represent the measured and true spectral densities respectively, r is the radius of a single transducer and U_c is the convection velocity. The tabulated data of Corcos for the attenuation of pressure fluctuations are also plotted in the same figure for comparison. The present data for pressure fluctuations, which were obtained numerically, agree fairly well with Corcos' results.

Corcos' analysis, however, is based on the decay rates $A(\omega\xi/U_c)$ and $B(\omega\eta/U_c)$ of the cross-spectral density introduced to fit the wall pressure data of Willmarth & Wooldridge (1962) which were obtained with a transducer of size $d^+ = 410$ at the rather high $Re_\theta = 29000$ (see table 2). The present investigation has been carried out with non-dimensional transducer size between 10 and 19 at lower R_θ. Since cross-spectral densities of pressure fluctuations, which could provide new estimates of A and B, were not measured, the validity of the present analysis was verified by using values of A and B from the work of Farabee & Casarella (1991) obtained with a transducer size of $d^+ = 33$. These experimental data show a faster decay than the data of Willmarth & Wooldridge. The results of the present analysis by using A and B functions based on the data of Farabee & Casarella are also shown in figure 4. The attenuation of the power spectral densities of pressure fluctuations predicted by using Farabee & Casarella's data is close to that predicted by using Willmarth & Wooldridge's values of A and B. The two predictions differ at higher frequencies. However, there is practically no difference between the two results for the vorticity flux. Both data sets of A and B values, although different by 70%, yield almost identical attenuation of vorticity flux. It appears therefore plausible to conclude that the

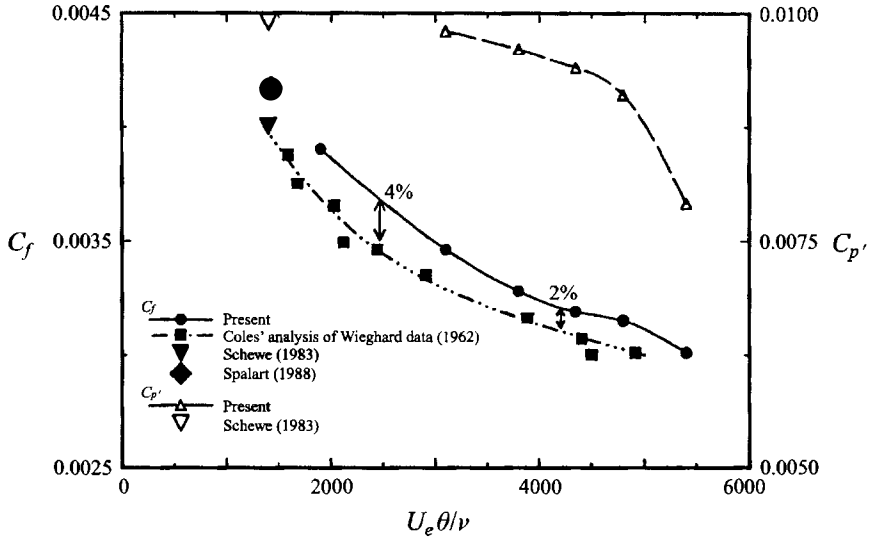

FIGURE 5. Pressure fluctuations and skin friction coefficient as a function of Re_θ.

estimates of the attenuation of vorticity flux obtained in the present study are not sensitive to large changes of A and B values.

It is evident that the attenuation of vorticity flux predicted by the present analysis is more pronounced than that of pressure. Hence, the true frequency spectrum of vorticity flux $\phi_t(\omega)$ for scales smaller than the probe size cannot accurately be recovered from measurements. Correction procedures may provide an estimate of the power spectral density in a frequency range over which the probe spatial resolution effects are important. No corrections have been applied to the present data.

4. Results

4.1. *Pressure fluctuation statistics and spectra*

In this section a comparison will be attempted between the present experimental results and existing data of other investigators. Figure 5 shows the root-mean-square (r.m.s.) pressure fluctuations normalized by the dynamic pressure of the free-stream flow $\frac{1}{2}\rho U_e^2$ as a function of the Reynolds number together with Schewe's (1983) data. The results clearly show a reduction of $c_{p'}$ with increasing Re_θ. The measured skin-friction values are also plotted on the same figure together with the results of Schewe (1983) and Spalart (1988), although the latter were obtained at different Re_θ. The present results are 2–4% higher than the values obtained by Cole's (1962) analysis of Weighard's data. It has been argued by Willmarth & Wooldridge (1962), and Willmarth (1975) that the ratio of r.m.s. pressure fluctuations to the local shear stress τ_w is always between 2 and 3. This has also been supported by more recent experimental results and direct numerical simulations. This ratio $p^+ = p'/\tau_w = p'/\rho u_\tau^2$ is plotted in figure 6(*a*) together with Schewe's experimental data and the results of Spalart's (1988) numerical simulations. As can be seen from this figure, the present data indicate a rather weak Reynolds number dependence of r.m.s. pressure fluctuation, particularly in the low-Re_θ region. Schewe's value obtained with a pressure transducer of diameter $d^+ = 21$ is considerably lower than Spalart's value at the same Re_θ, but only slightly lower than

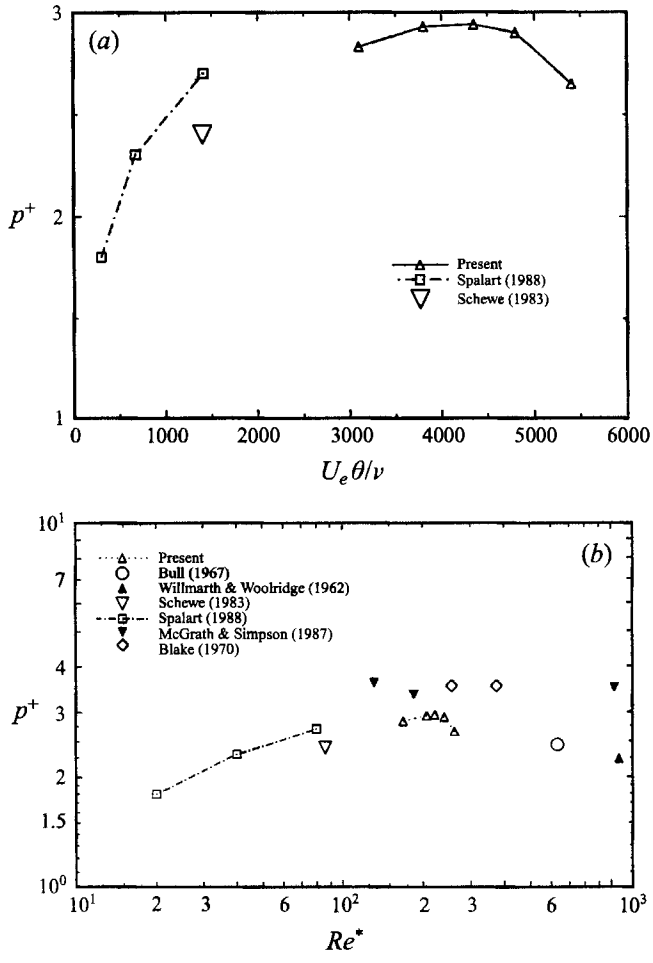

FIGURE 6. Pressure fluctuations scaled by inner wall variables as a function of (*a*) Re_θ, (*b*) $Re^* = \delta^*/\nu$.

the present value of p^+ at the highest $Re_\theta = 5400$ which was obtained with a transducer of comparable resolution, $d^+ = 19$.

It has been argued by Bradshaw (1967) that the -1 slope of the frequency spectra suggests that p^+ is a function $u_\tau\delta/\nu$, i.e. of the outer to inner scale ratio of the boundary-layer flow. This ratio, however, is better expressed in terms of $u_\tau\delta^*/\nu$ where δ^* is the displacement thickness. Figure 6(*b*) shows the dependence of p^+ on $Re^* = u_\tau\delta^*/\nu$. The data of McGrath & Simpson (1987) and Blake (1970) do not demonstrate any Re^* dependence. In addition they are considerably higher than the rest of the data under comparison. The present experimental data together with the data of Spalart and Schewe clearly follow the same pattern, indicating that p^+ increases with Re^*. The data of Bull (1967) and Willmarth & Wooldridge (1962) suggest a different trend. These data, however, have been obtained with relatively large pressure transducers, $d^+ = 173$ and 410 respectively. Schewe (1983) and more recently Keith, Hurdis & Abraham (1992) have shown that poor spatial resolution can lead to substantial errors in estimating pressure fluctuation r.m.s. and spectral densities. In that respect these data should be treated with considerable caution. Comparison of the present data with data obtained in channels has not been attempted here because the work of Keith *et al.* (1992) has indicated that considerable difference exists in the

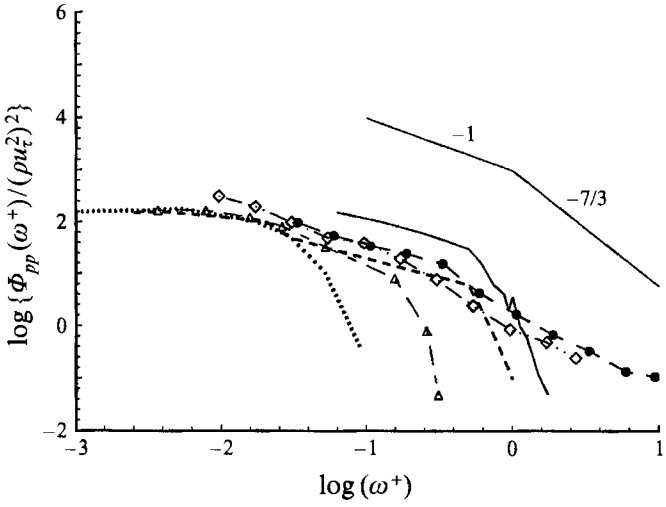

FIGURE 7. Power spectral densities of pressure fluctuations scaled by inner wall variables. See table 2 for symbols.

Investigation	Re_θ	d^+	Symbols
Willmarth & Wooldridge (1962)	29000	410	— — △ — —
Hasan *et al.* (1986)	3389	505	.....
Devenport *et al.* (1990)	7590	33 (estimated)	— — — — —
Haritonidis *et al.* (1988)	4340	19	———
Present Exp. 1	3100	10	●-●-●-●-●
Present Exp. 6	5400	19	-◇-◇-◇-◇-◇-

TABLE 2. Data for experiments shown in figure 7

spectral levels of pressure fluctuations between external flows like a boundary layer and internal flows like a channel flow.

Typical power spectral densities (p.s.d.) for the two Re_θ, 3100 and 5400, of the present data are shown in figure 7 plotted in terms of inner wall variables. The data of Willmarth & Wooldridge (1962), Hasan, Casarella & Rood (1986), and Devenport *et al.* (1990) are also plotted for comparison. All the data have been obtained in different facilities under different conditions, pressure transducer sizes and equipment. Table 2 shows the transducer size and the corresponding Re_θ of these experiments. Microphones were used in all cases except the present one. As can be seen from figure 7, the present data agree fairly well with the results of the previously mentioned investigations bearing in mind the uncertainties involved, such as background noise and inadequate spatial resolution. The results of the present investigation for the two Re_θ shown in figure 7 agree fairly well with each other particularly in the low-frequency range, $\omega^+ < 0.2$.

In the region $\omega^+ > 0.2$ the p.s.d. values of the high-Re_θ experiment seem to fall off slightly faster than the low-Re_θ case, most probably due to the difference in the spatial resolution of scales. The same figure also shows the ω^{-1} and $\omega^{-7/3}$ variations normally expected in two-dimensional boundary-layer flows. The present results for both Re_θ values and the results of Willmarth & Wooldridge show a large region of ω^{-1} variations as suggested by Bradshaw (1967) and Kim (1989) and a rather short region of $\omega^{-7/3}$ as suggested by Schewe (1983). In fact the present p.s.d. values seem to exhibit a $\omega^{-7/4}$

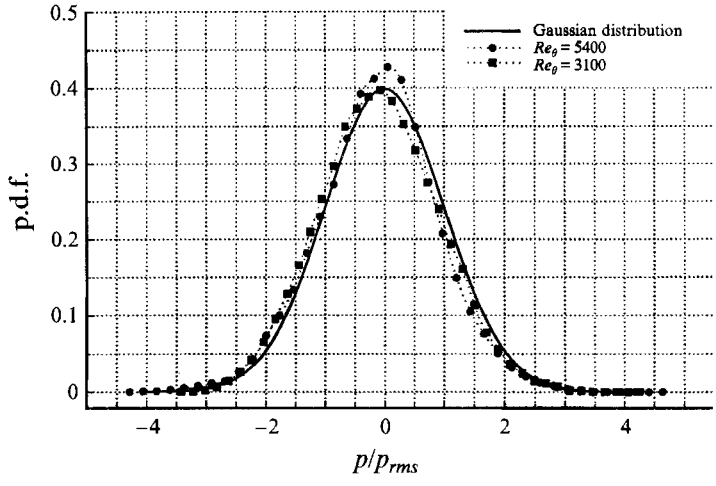

FIGURE 8. Probability density function of pressure fluctuations.

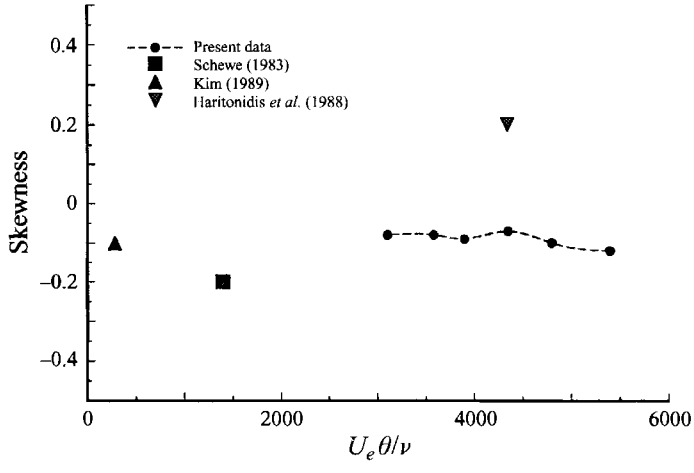

FIGURE 9. Skewness of pressure fluctuations as a function of Re_θ.

power law in the high-frequency part of the spectrum $\omega^+ > 0.3$ where the flow may be locally isotropic. It should be noted that Panton & Gilles (1992) suggest a -2 slope for the viscosity-dominated equilibrium region of the spectrum. It is not at all certain that such an equilibrium region exists in the present spectra. The fact, however, that the slope $-7/4$ of the present data is less than -2 suggests that this region could be traced at higher ω^+ if greater resolution were available.

Figure 8 illustrates the probability density function (p.d.f.) of pressure fluctuations at two different Re_θ. The Gaussian distribution is also plotted for comparison. The present results clearly show that there is an asymmetry in the distribution at both Re_θ, indicating that the probability of higher negative values of pressure amplitudes is somewhat greater than the probability of positive values of pressure amplitudes. This is also indicated by the skewness of pressure fluctuations plotted in figure 9. All present experimental data as well as the data of Schewe (1983) and the direct numerical simulation results of Kim (1989) exhibit a negative skewness. Haritonidis *et al.*'s (1988) data indicate a positive value of the skewness although their probability densities are

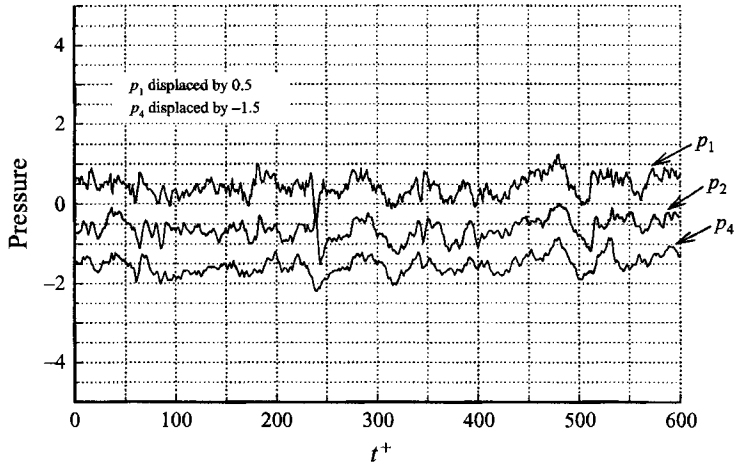

FIGURE 10. Typical pressure signals, $Re_\theta = 5400$. p_1 is displaced by 0.5 units, p_2 by -0.5 and p_4 by -1.5.

clearly skewed towards the negative values. Another significant characteristic, which was first observed by Schewe (1983) and Haritonidis *et al.* (1988) is that the appearance of extremely low and high amplitudes of pressure fluctuations is more frequent than in a process obeying a Gaussian distribution. Large-amplitude fluctuations of the order of $\pm 5\ p_{r.m.s.}$ have been observed in the present investigation as well as in the experiments of Schewe and Haritonidis *et al.* They may be associated with intermittent phenomena of significant importance in the near-wall region. Kim (1989) and Spalart (1988) noticed that a strong correspondence exists between low-pressure regions and streamwise vortices. It is possible that the intermittent appearance of low-pressure fluctuations in the p.d.f. is associated with the vortices present in the flow.

It is obvious that the results of this investigation presented so far do not show a strong Re_θ dependence. In addition, the good agreement of the present pressure statistics and power spectral densities with those obtained by other researchers in different facilities and under different conditions, first suggests that the present boundary-layer flow follows the expected behaviour and secondly provides confidence in the techniques applied and probes used in this investigation and improves the credibility of the measurements of vorticity fluxes away from the wall.

4.2. *Vorticity flux signals and statistics*

The pressure signals from transducers 1, 2 and 4 were used to compute the pressure gradients shown in equation (11) and subsequently the vorticity gradients $\partial\omega_x/\partial y$ and $\partial\omega_z/\partial y$ were evaluated at the wall. Figure 10 shows some typical pressure signals obtained at $Re_\theta = 5400$ and figure 11 illustrates the corresponding vorticity gradients/fluxes. The values of pressure and time have been non-dimensionalized by using inner-layer scaling. When examining the simultaneous pressure traces for similarities it was obvious that all signals were highly correlated. A common way of characterizing the degree of correlation is to compute the correlation coefficient defined as

$$R_{ij} = \frac{\overline{p_i p_j}}{[\overline{p_i^2}]^{1/2}[\overline{p_j^2}]^{1/2}}. \tag{14}$$

Coefficients with values between 0.86 and 0.91 have been obtained in the present experiments. The resultant vorticity gradient/flux signals are for some reason

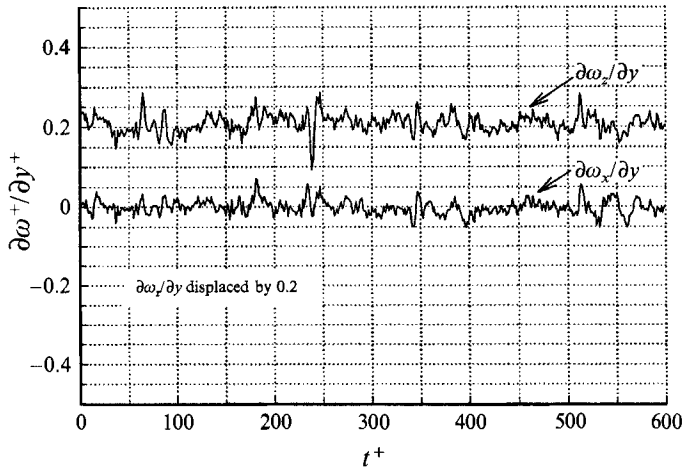

FIGURE 11. Typical vorticity gradient signals, $Re_\theta = 5400$.

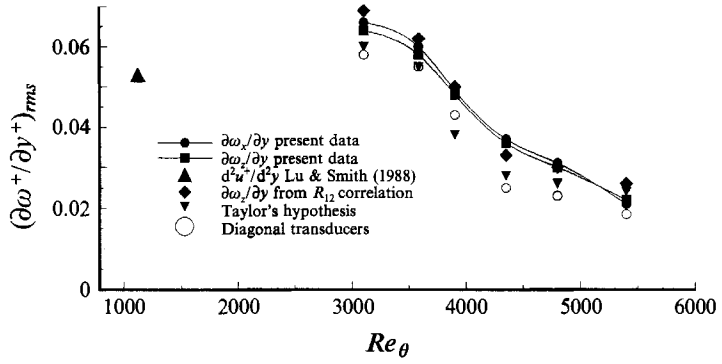

FIGURE 12. Statistics of vorticity flux fluctuations: r.m.s. variation with Re_θ (inner wall scaling).

correlated to a lesser extent than the pressure signals. They indicate some intense vortical activities on the wall without any time intervals of no activity. Another characteristic of these signals is that each signal spends time on the positive as well as on the negative side confirming that a solid wall can act as a source as well as a sink of vorticity.

The statistics of the vorticity-flux signals at various Re_θ are plotted in figure 12, 15, 16 and 17. Figure 12 illustrates the r.m.s. variation of the vorticity gradients with Re_θ. The results indicate a rather strong dependence of these gradients on Re_θ, which may suggest a possible breakdown of inner wall scaling. Although the spatial resolution of the probe is deteriorating with increasing Re_θ it cannot account for the sharp fall of the r.m.s. at high Re_θ. It is interesting to observe that while pressure fluctuations scale rather satisfactorily with inner wall variables, pressure gradient/vorticity flux fluctuations do not.

Since the present measurements of vorticity flux are, to the best of our knowledge, the first of their kind, no previous data exist for direct comparison. There is however an estimate of the r.m.s. of the gradient $\partial^2 u^+/\partial y^{+2}$ at the wall obtained by Lu & Smith (1983). This is also plotted in figure 12. These authors measured this velocity derivative near to the wall by using hot wires and hot films. Then, by using orthogonal decomposition, they calculated the r.m.s. of this derivative inside the flow and

extrapolated these values to the wall, finding a value of 0.053 at the wall. They considered these values to be underestimates of the true values because very few eigenmodes were included in the decompositions. In fact these values, at positions just off the wall inside the flow, are 30–50% lower than the measured values. After considering this, it appears that the present data compare satisfactorily with the estimate of Lu & Smith (1988).

In order to obtain independent estimates of the r.m.s. of vorticity gradients at the wall from the present data, several alternative methods have been attempted. First, the values of the cross-correlation coefficient R_{ij} have been used to compute the r.m.s. of vorticity flux. Consider, for instance, the pressure difference p_2-p_1 and its r.m.s.

$$[\overline{(p_2-p_1)^2}]^{1/2} = [\overline{p_2^2}+\overline{p_1^2}-2R_{12}(\overline{p_2^2})^{1/2}(\overline{p_1^2})^{1/2}]^{1/2}.$$

Since $\overline{p_2^2} \approx \overline{p_1^2}$ then

$$[\overline{(p_2-p_1)^2}]^{1/2} = [2(1-R_{12})(\overline{p_1^2})]^{1/2}.$$

By considering that

$$\frac{\partial \omega_z^+}{\partial y^+} = -\frac{\partial p^+}{\partial x^+}$$

it can be shown that

$$\left\{\frac{\partial \omega_2^+}{\partial y^+}\right\}_{r.m.s.} \approx \frac{[2(1-R_{12})]^{1/2}}{\Delta x^+} p^+. \tag{15}$$

Thus the r.m.s. of vorticity flux can be obtained from the measurements of R_{12} and the r.m.s. of pressure fluctuations. These results are plotted in figure 12. They agree remarkably well with the data obtained directly from the pressure gradients described by (11).

A second estimate of the r.m.s. of vorticity flux has been obtained by considering the pressure gradients in the diagonal directions as indicated by equation (13) and then transforming the time-dependent data into the *xoz* coordinate system. The results of this are also plotted in figure 12. It appears that they are lower than both previous estimates: those obtained from the pressure gradients in the original *xoz* coordinates and those obtained from the cross-correlation data. The difference is about 14% at the low Re_θ and about 25% at the highest Re_θ. This discrepancy, however, is not surprising since signal attenuation has resulted from a deterioration in spatial resolution. In the case of diagonal pressure gradients the separation between the pressure transducers has been increased by a factor of $\sqrt{2}$ in comparison to the original case and, therefore, considerable attenuation of the signals is expected as is also predicted by the theory.

At the suggestion of one referee, a fourth estimate of vorticity-flux r.m.s. has been obtained by invoking Taylor's hypothesis of 'frozen' turbulence convection on the time-dependent pressure signal. Taylor's hypothesis is a direct outcome of the Navier–Stokes equations if all viscous terms and pressure gradients are extremely small in comparison to the convection terms during the short times of interest:

$$\frac{\partial U}{\partial t}+U\frac{\partial U}{\partial s} \approx 0 \quad \text{then} \quad \frac{\partial U}{\partial s} \approx -\frac{1}{U_c}\frac{\partial U}{\partial t}, \tag{16}$$

where s is the direction along a streamline and U_c is the convection velocity. Although pressure may not be a quantity easily described by a transport equation, and despite the fact that any convection velocity U_c at the wall is zero, a relation equivalent to (16) can be assumed to hold for pressure:

$$\frac{\partial p^+}{\partial x^+} = -\frac{1}{C^+}\frac{\partial p^+}{\partial t^+}, \tag{17}$$

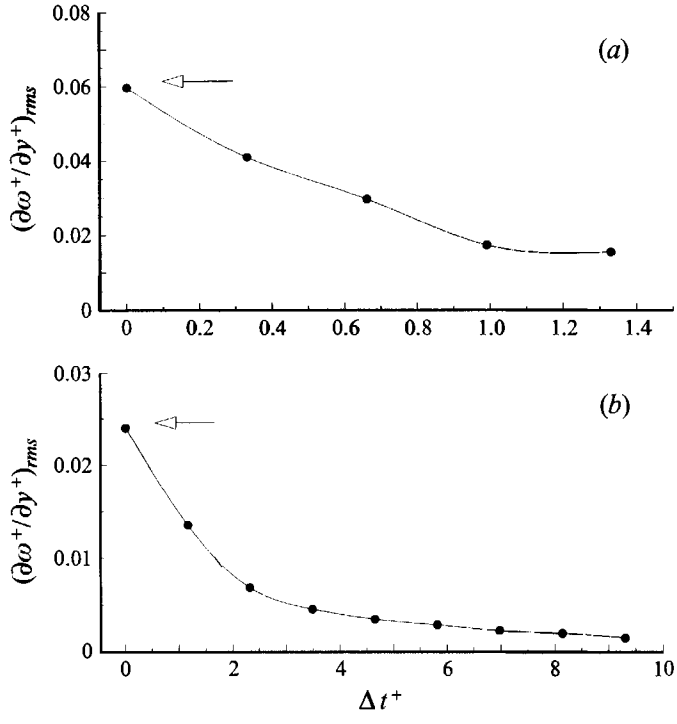

FIGURE 13. Statistics of vorticity flux fluctuations obtained from pressure signals by applying Taylor's hypothesis: r.m.s. variation with Δt^+ (inner wall scaling) for (*a*) $Re_\theta = 3100$, (*b*) $Re_\theta = 5400$.

if a propagation velocity C^+ is used instead of a convection velocity. Thus all statistical information on the time derivative of the pressure signal can be transformed into statistical information on the longitudinal pressure gradient. In the present case the time derivative has been approximated by the following finite-difference scheme:

$$\frac{\partial p^+}{\partial t^+} \approx \frac{[p(t^+ + \Delta t^+) - p(t^+)]}{\Delta t^+}. \tag{18}$$

The same referee suggested the use of different time separations Δt^+ in this analysis to find out how the values vary as Δt^+ approaches zero. The present pressure data have been reanalysed to compute all vorticity-flux statistics from the time derivative of pressure. Typical results indicating how the r.m.s. and skewness vary with Δt^+ are shown in figures 13(*a*, *b*) and 14(*a*, *b*) for $Re_\theta = 3100$ and $Re_\theta = 5400$ respectively. The smallest value of Δt^+ used is that of the digital sampling interval shown in table 1. Multiples of the sampling interval were used for higher values of time separation Δt^+. In the present analysis a value of 12.5 has been assigned to C^+ which is close to what has been found by Moin & Kim (1985). It should be noted that flatness and skewness are independent of the value of C^+.

The effect of different spatial/temporal resolution, as indicated by varying Δt^+, is not the same for all statistical quantities of vorticity flux. The r.m.s. values, for instance, shown in figures 13(*a*) and 13(*b*), seem to depend strongly on Δt^+, while skewness, shown in figures 14(*a*) and 14(*b*), as well as flatness, are much less sensitive to Δt^+. The results shown in figures 13(*a*) and 13(*b*) clearly demonstrate that there is a threshold value of Δt^+, Reynolds number dependent, below which a very substantial change in the r.m.s. can be observed. These thresholds appear to be $\Delta t^+ \approx 1$ for $Re_\theta = 3100$ and

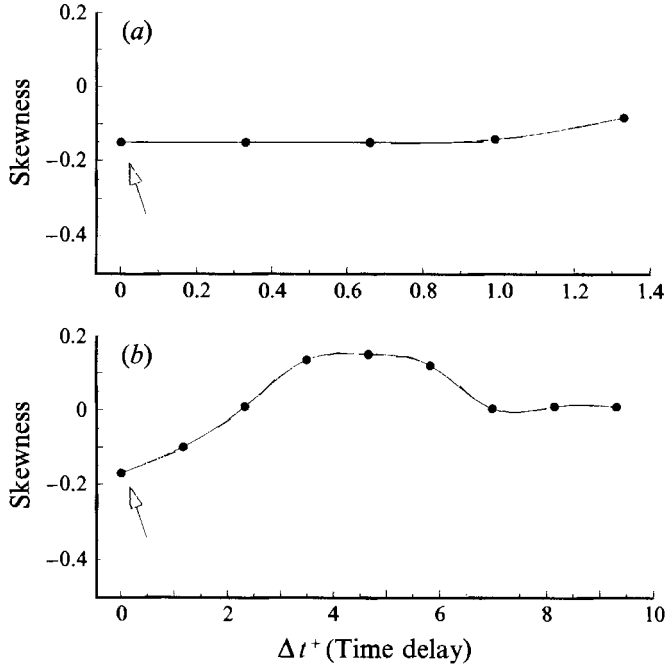

FIGURE 14. Statistics of vorticity flux fluctuations obtained from pressure signals by applying Taylor's hypothesis: r.m.s. variation of skewness with Δt^+ (inner wall scaling) for (*a*) $Re_\theta = 3100$, (*b*) $Re_\theta = 5400$.

$\Delta t^+ \approx 3.5$ for $Re_\theta = 5400$. For values of Δt^+ greater than these thresholds there is no significant change in the values of all statistical quantities of vorticity flux. The skewness values of the lowest $Re_\theta = 3100$ case, shown in figure 14(*a*), are almost independent of Δt^+, while the skewness values of the $Re_\theta = 5400$ case, are affected more. Nevertheless, this analysis shows that several statistical quantities of vorticity flux may be seriously underestimated by inadequate spatial or temporal resolution.

The values finally adopted according to the present procedures are indicated by an arrow in the figures described above. These values are the results of extrapolation of the present data down to $\Delta t^+ = 0$. They are also plotted in figure 12 for comparison with the results obtained by considering longitudinal or diagonal pressure gradients and the cross-correlation data R_{12}. It appears that they agree rather well with these data, particularly in the high-Re_θ cases.

The relatively good agreement among the various estimates of r.m.s. values of vorticity flux obtained by four different methods first indicates a high degree of internal consistency of the present data and second provides confidence in the experimental techniques used to measure and resolve this quantity.

Further insight into the physics of vorticity flux can be obtained by looking at (15) which shows the dependence of the r.m.s. value on the cross-correlation coefficient R_{12}. It can be noted that the r.m.s. value of the vorticity gradients consists entirely of contributions from the uncorrelated part of the two pressure signals which may be expressed as $(1-R_{12})$. This indicates that if the two pressure signals are 100% correlated there is no vorticity flux away from the wall. The same relation (15) also explains the strong dependence of the r.m.s. of vorticity flux on Re_θ. By considering this equation it can be argued that the r.m.s. of the vorticity gradient varies with Re_θ as $1/\Delta x^+$ does. This follows from our results of figure 6(*a*) which shows that p^+ is quite

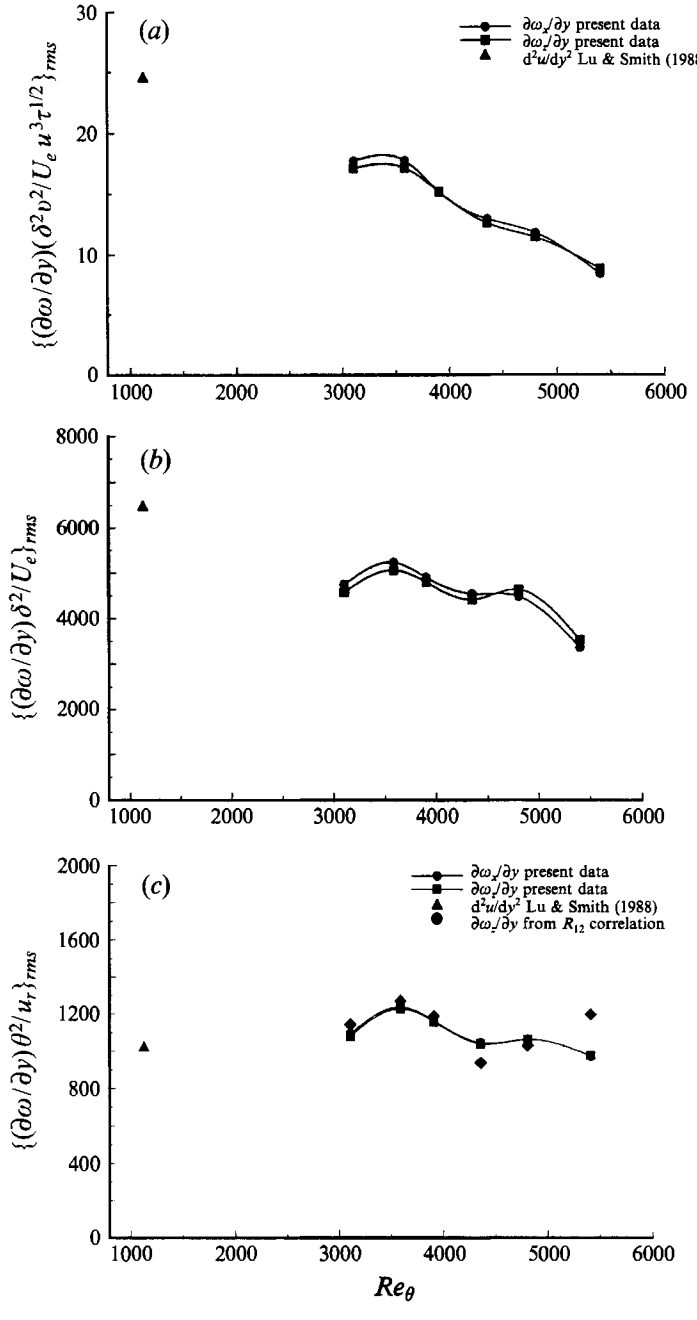

FIGURE 15. Statistics of vorticity flux fluctuations: r.m.s. variation with Re_θ for (*a*) mixed scaling, (*b*) outer wall scaling and (*c*) scaled with u_τ and θ.

independent of Re_θ in the investigated range and R_{12} changes slightly with Re_θ, suggesting that the numerator $2(1-R_{12})^{1/2}p^+$ is a rather weak function of Re_θ. Since Δx^+ increases fast with increasing Re_θ (see table 1), $(\partial\omega_z^+/\partial y^+)_{r.m.s.}$ should decrease rather quickly with Re_θ.

Thus it appears that this strong Reynolds number dependence is genuine. Reynolds number effects on turbulence statistics have been the subject of considerable

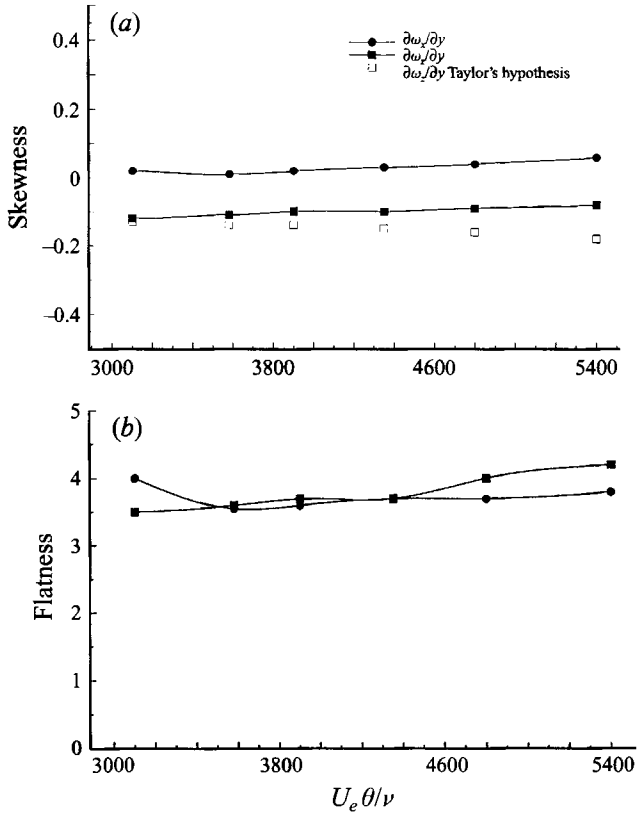

FIGURE 16. Statistics of vorticity flux fluctuations: variation with Re_θ of (*a*) skewness and (*b*) flatness.

investigations. The recent review of Gad-el-Hak & Bandyopadhyay (1994) indicates that these effects are more pronounced on higher-order statistics. Andreopoulos, Durst & Jovanovic (1984), for instance, have reported that Reynolds number effects on flatness and skewness of streamwise velocity fluctuations have penetrated the boundary layer all the way down to the edge of the viscous sublayer. The present data for vorticity flux shows a much stronger effect of Reynolds number dependence. Consequently it is plausible to assume that the inner-layer variable ν^2/u_τ^3 does not provide the appropriate scaling for the vorticity-flux data. Figures 15(*a*) and 15(*b*) show plots of the same data non-dimensionalized with the mixed and outer scales respectively. The outer variables δ and U_e give U_e/δ^2 as a typical vorticity-flux scale while the mixed scale is the geometric mean of inner and outer scales, i.e.

$$\left[\frac{\nu^2}{u_\tau^3}\frac{\delta^2}{U_e}\right]^{1/2}.$$

Neither type of scaling provides any satisfactory collapse of the data. If however the momentum thickness θ is used as a lengthscale and the friction velocity u_τ as a velocity scale then the vorticity-flux data, shown in figure 15(*c*), are less spread out than with any other scaling. They collapse reasonably well to a value

$$\frac{\partial\omega_z}{\partial y}\frac{\theta^2}{u_\tau} \approx 10^3.$$

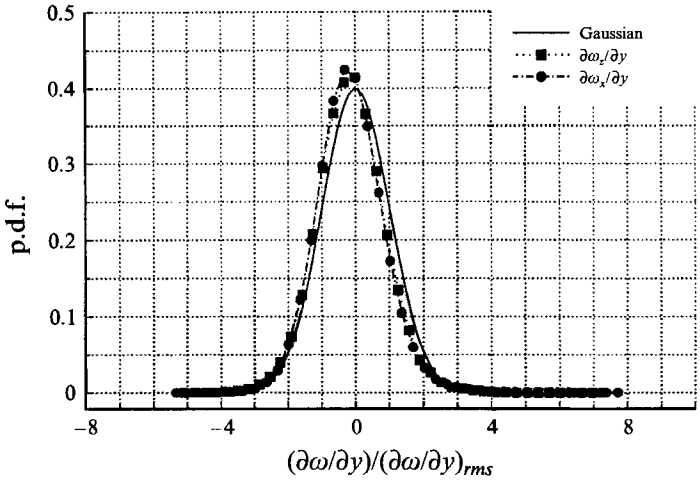

FIGURE 17. Probability density function of vorticity flux fluctuations, $Re_\theta = 3100$.

The skewness and flatness of the vorticity flux derivative signal, plotted in figures 16 and 16(*b*) respectively, show no Re_θ-dependence. The skewness of $\partial\omega_z/\partial y$ has a negative value of slightly less than -0.1 averaged over the entire range of Re_θ, while the skewness of $\partial\omega_x/\partial y$ reaches small positive values. Also plotted in this figure are the skewness data obtained from the pressure signals by applying Taylor's hypothesis. These data, which are independent of the value of propagation velocity, also indicate a rather weak Re_θ effect. The values of flatness for both gradients are between 3.6 and 4.2, indicating the existence of rather rare events of strong amplitude followed by extended periods of activities of moderate amplitudes.

In figure 17 the probability density distribution of the two vorticity gradients are illustrated for the case $Re_\theta = 3100$. The Gaussian distribution is also plotted for comparison. It is obvious that the distribution of the present experimental data significantly deviates from the Gaussian one. However, the most striking feature of the data is the presence of extremely high and low amplitudes of both vorticity gradients which, although having low probability of appearance, contribute significantly to the statistics. This indicates that the fluid acquires or loses vorticity at the wall during some rather violent events followed by periods of rather small fluctuations. The same behaviour has been observed in all the experiments at different Re_θ. The maximum amplitude in the signals observed is $9(\partial\omega/\partial y)_{r.m.s.}$ while the minimum was $-7(\partial\omega/\partial y)_{r.m.s.}$. Had the spatial resolution of the probe been inadequate none of these events could have been detected.

Another noticeable characteristic of the vorticity-flux signals is the behaviour of the intermittency factor which indicates the percentage of time the signal spends on the positive or negative side. The present analysis shows that $\partial\omega_z/\partial y$ is positive for 49.5% of the time while the rest of the time it is negative. The intermittency values for the $\partial\omega_x/\partial y$ signal are similar. It has been also found that these values are independent of Re_θ. These facts suggest that roughly half of the time the wall acts like a source of vorticity and for the other half it acts like a sink of vorticity.

The correlation coefficient between the two components of σ_w was found to be very small, of the order of 0.014. This low value is not a surprise because symmetry considerations for the present flow suggest that there is no correlation between the two components.

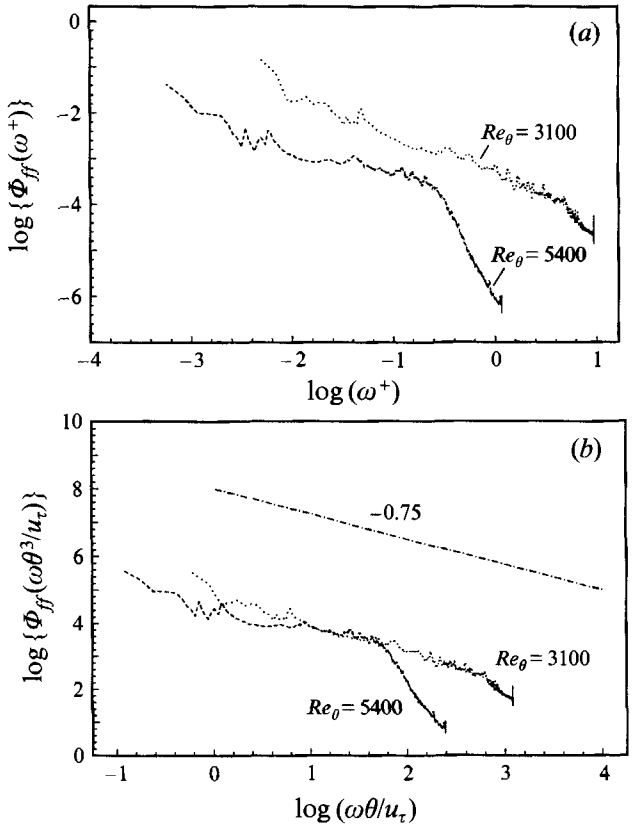

FIGURE 18. Power spectral densities of vorticity flux scaled by (*a*) inner wall variables and (*b*) u_τ and θ. ·····, $Re_\theta = 3100$; -----, $Re_\theta = 5400$.

Figure 18(*a*) shows the power spectral densities $\Phi_{ff}(\omega^+)$ of the vorticity flux $\partial\omega_z/\partial y$ at two different Reynolds numbers. No appreciable peaks can be discerned in any frequency region while a very strong Reynolds number effect is noticeable. In view of the results shown in figure 12 this behaviour may be expected. If, however, the suggested type of scaling is used, the spectral densities are brought very close. Figure 18(*b*) depicts the data scaled with u_τ and θ. As can be seen, they collapse fairly well over a relatively wide range of frequencies except at very high frequencies where limitation of spatial resolution in the case of high Re_θ may be present. Another feature emerging from this figure is the $(\omega\theta/u_\tau)^{-0.75}$ variation of the collapsed data. The present dual scaling, although fundamentally different from the classical mixed scaling, is essentially a mixture of inner- and outer-layer scaling. This scaling has been found by Alfredsson & Johansson (1984), Shah & Antonia (1989) and Naguib & Wark (1992) to scale the bursting frequency satisfactorily over a rather wide range of Reynolds number variation.

The results of the present investigation indicate that one scale may not be enough to describe all quantities or events in a turbulent boundary layer. Particularly, the vorticity-flux data suggest that wall events associated with vorticity production follow a mixed-layer type of behaviour indicating that there is an outer-layer influence on the wall.

5. Transport equations

The effort to understand the dynamically significant physical phenomena involved in near-wall turbulence through vorticity-flux measurements requires consideration of the transport equation for vorticity and strain. The incompressible Navier–Stokes equations after proper differentiation are equivalent to a coupled set of transport equations for vorticity ω_i and the strain tensor $S_{ik} = \frac{1}{2}(\partial u_i/\partial x_k + \partial u_k/\partial x_i)$. The equation for ω_i in a Lagrangian frame is

$$\frac{\mathrm{D}\omega_i}{\mathrm{D}t} = S_{ik}\,\omega_k + \nu\frac{\partial^2\omega_i}{\partial x_k\,\partial x_k}, \tag{19}$$

where $\mathrm{D}/\mathrm{D}t = \partial/\partial t + u_k\,\partial/\partial x_k$ is the total derivative. Differentiation of the above equation in the direction x_2 normal to the wall leads to the following transport equation for the vorticity flux $\sigma_{i2} = \partial\omega_i/\partial x_2$:

$$\frac{\mathrm{D}\sigma_{i2}}{\mathrm{D}t} = S_{ik}\,\sigma_{k2} - \frac{\partial u_k}{\partial x_2}\sigma_{ik} + \omega_k\frac{\partial S_{ik}}{\partial x_2} + \nu\frac{\partial^2\sigma_{i2}}{\partial x_k\,\partial x_k}. \tag{20}$$

The deformation rate $\partial u_k/\partial x_2$ can be split into its symmetric part S_{k2} and antisymmetric part $-\frac{1}{2}\epsilon_{k2j}\,\omega_j$ where ϵ is the alternating tensor, ϵ_{ijk}, being 1 if i,j,k are in cyclic order, -1 if i,j,k are in anticyclic order and 0 otherwise. Then

$$\frac{\mathrm{D}\sigma_{i2}}{\mathrm{D}t} = \sigma_{k2}\,S_{ik} - \sigma_{ik}\,S_{k2} + \omega_k\frac{\partial S_{ik}}{\partial x_2} + \epsilon_{k2j}\,\omega_j\,\sigma_{ik} + \nu\frac{\partial^2\sigma_{i2}}{\partial x_k\,\partial x_k}. \tag{21}$$

The dynamically significant processes associated with vorticity are the amplification and rotation of the vorticity vector by the strain $\boldsymbol{S}$ and vortex tearing at very small scales due to viscosity which may induce reconnection of the vortex. The dynamical equation for vorticity flux σ_{i2} is more complex: There are in general four 'source' or 'sink' terms in addition to the smoothing term, which express amplification and attenuation of vorticity flux by the strain $\boldsymbol{S}$, rotation due to vorticity and nonlinear interaction between vorticity and gradients of strain.

It is remarkable to observe that the strain tensor $\boldsymbol{S}$ plays a role in the transport of vorticity flux σ similar to that in the transport equation of vorticity ω. The solenoidal characteristic of vorticity, $\partial\omega_i/\partial x_i = 0$, results in a similar feature for vorticity flux. This can be seen by differentiating (21) in the x_k direction:

$$\frac{\partial}{\partial x_k}\left(\frac{\partial\omega_i}{\partial x_i}\right) = 0,$$

and interchanging the order of differentiation provided that ω_i is a continuous function. This leads to

$$\frac{\partial}{\partial x_i}\sigma_{ik} = 0.$$

We can also obtain the transport equation for the instantaneous $\frac{1}{2}\sigma_{i2}^2$ by multiplying (21) by σ_{i2} and splitting the viscous term into diffusive and dissipative parts:

$$\frac{\mathrm{D}}{\mathrm{D}t}(\tfrac{1}{2}\sigma_{i2}^2) =$$

$$\sigma_{i2}\,\sigma_{k2}\,S_{ik} - \sigma_{i2}\,\sigma_{ik}\,S_{k2} + \sigma_{i2}\,\epsilon_{k2j}\,\omega_j\,\sigma_{ik} + \sigma_{i2}\,\omega_k\frac{\partial S_{ik}}{\partial x_2} + \nu\frac{\partial^2}{\partial x_k\,\partial x_k}(\tfrac{1}{2}\sigma_{i2}^2) - \nu\left(\frac{\partial\sigma_{i2}}{\partial x_k}\right)\left(\frac{\partial\sigma_{i2}}{\partial x_k}\right). \tag{22}$$

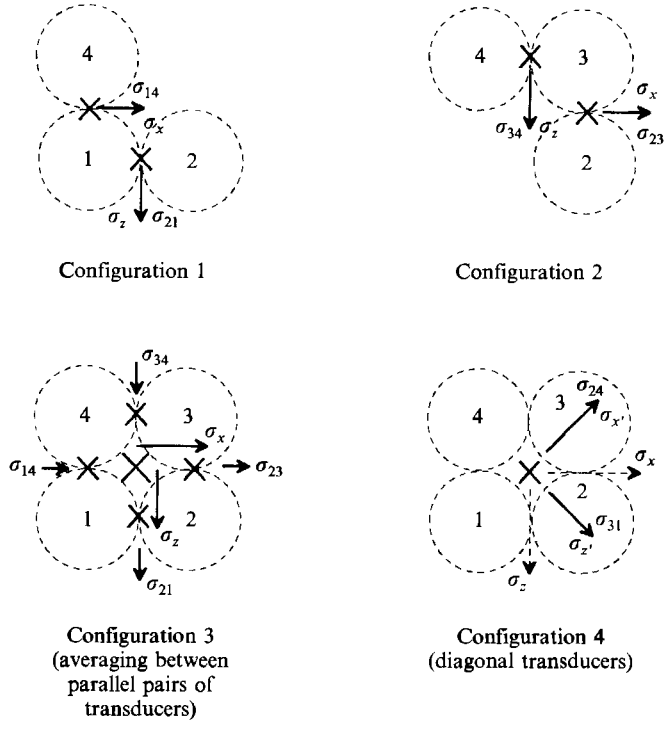

FIGURE 19. Configurations of transducer arrays.

The term on the left-hand side of (22) can be interpreted as the advection term while the first four terms on the right-hand side can be interpreted as the amplification or attenuation of $\frac{1}{2}\sigma_{i2}^2$. The presence of the strain $\boldsymbol{S}$ in three out of four of these terms indicates the significance of vortex line stretching and compression by this strain in the generation of vorticity-flux fluctuations. Thus vortex line stretching causes not only vorticity but also vorticity flux changes.

6. Two-component analysis

The availability of four simultaneous signals from the pressure transducers leads to the two-component analysis of their gradients. A key quantity which may help understand the near-wall turbulence is the orientation of the vorticity flux vector on the wall, $\boldsymbol{\sigma}_w$. Four different combinations among the four transducers were used in this analysis, which are shown in figure 19. Configuration 1 combines three transducers, 1, 2 and 3, to compute σ_{12} and σ_{14} at the mid-points between the centres of the pressure transducers. Similarly, transducers 2, 3 and 4 were used to calculate σ_{23} and σ_{34} on configuration 2. Configuration 3 utilizes all four transducers and the resultant components are the averages of the parallel transducers pairs, $\sigma_x = \frac{1}{2}(\sigma_{14}+\sigma_{23})$ and $\sigma_z = \frac{1}{2}(\sigma_{21}+\sigma_{34})$. The diagonal transducers were used in the last configuration 4. It should be noted that in the first two asymmetric configurations the two components do not act at the same point while in the last two symmetric ones the resultant components act at the centre of the array, i.e. at the origin of the coordinate system. As will be shown, the two asymmetric configurations impose a bias in the directional sensitivity of the transducer array.

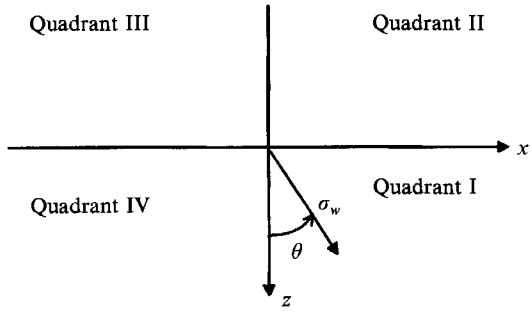

FIGURE 20. Definition of angular orientation of wall vorticity flux vector σ_w.

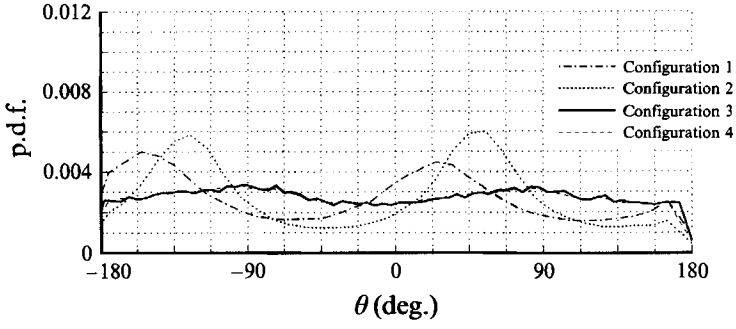

FIGURE 21. Probability density function of orientation θ of vorticity flux vector σ_w.

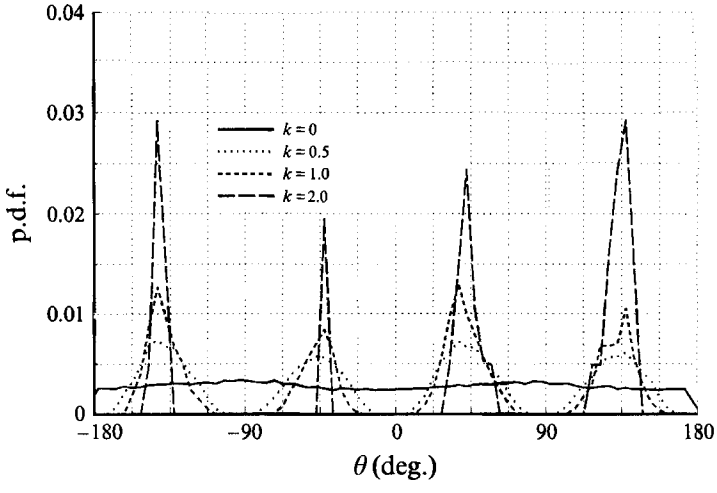

FIGURE 22. Conditional probability density function of orientation θ of vorticity flux vector σ_w.

If θ is the angle between $\boldsymbol{\sigma}_w$ and the positive z-axis as shown in figure 20 then $\theta = \tan^{-1}(\partial\omega_x/\partial y/\partial\omega_z/\partial y) \approx \tan^{-1}(\Delta\omega_x/\Delta\omega_z)$. θ is positive in the anticlockwise direction and varies in the range $-180° < \theta < 180°$. Statistical analysis of θ showed a large r.m.s. value, of the order of 100°, which is indicative of a highly fluctuating vector orientation. The distribution of the probability density function of θ has been computed for the four different transducer configurations and is shown in figure 21.

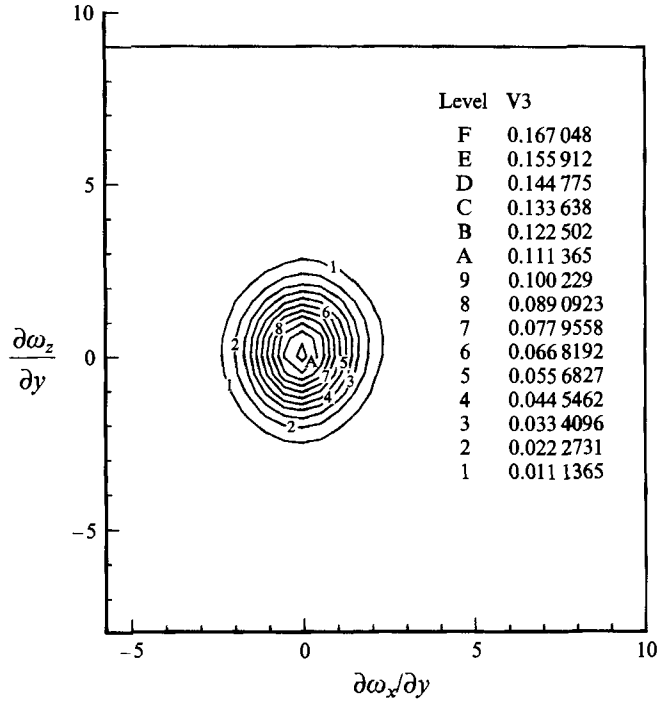

FIGURE 23. Iso-probability contours for $Re_\theta = 3100$.

The two asymmetric configurations exhibit two peaks at about 45° and −135° while the two symmetrical ones are identical. The symmetry requirements of the present flow suggest that the distribution of θ should be symmetric about the longitudinal axis, i.e. about $\theta = 90°$ and $-90°$. The two asymmetric configurations clearly do not possess this characteristic while configurations 3 and 4 indicate the expected symmetric distribution. In the asymmetric configurations one pressure signal is common in the calculation of both pressure gradients. Most likely this increases the correlation between the two pressure gradients which results in the skewed distribution of p.d.f. It is obvious that the two symmetric configurations suppress this directional sensitivity bias which is evident in the asymmetric ones. The analysis, therefore, of the two components was performed by using configurations 3 and 4. Although these two configurations gave identical results in the p.d.f. of θ, configuration 3 was finally used to compute the results shown here because of its better spatial resolution in the measurements of each individual pressure gradient.

Of particular interest is the orientation of σ_w during the violent events which are associated with large excursions in amplitude. In order to further investigate the behaviour of these events, conditional sampling analysis has been applied to the vorticity flux signals $\partial\omega_x/\partial y$ and $\partial\omega_z/\partial y$. An 'event' was detected when the absolute value of each of the two signals was above a threshold level set at a fraction or multiple of the r.m.s. value, $k(\partial\omega/\partial y)_{r.m.s.}$. Subsequent interrogation of the sign of each signal determined the corresponding algebraic value of θ according to the above definition. Figure 22 shows p.d.f.'s of θ for various values of the threshold level k: 0, which corresponds to the original unconditioned data, 0.5, 1.0 and 2.0. It is very remarkable to observe that the application of the lowest threshold, $k = 0.5$, changes significantly the distributions by filtering out all small-amplitude contributions and reveals a certain

organization in the distribution: large amplitude events are oriented in preferential directions of rather narrow bands, one in each quadrant at $\theta = \pm 45°$ and $\pm 135°$. It should be noted that the biasing effect produced by the asymmetric configuration 1 diminishes the events occurring in the II and IV quadrants.

There is a propensity of alignment between vorticity and eigenvectors of the strain-rate tensor S_{ij} which has been shown to take place in the numerical simulations of isotropic and homogeneous turbulent flows by Ashurst *et al.* (1987) and in the experimental investigation of vortical structures near the wall in turbulent boundary layers by Honkan (1994). It is very likely that the most probable orientation found in the present experimental analysis is closely related to the eigenvectors of the strain-rate tensor S_{ij} at the wall.

Figure 23 shows the iso-probability contours obtained from the joint probability density function of the two pressure gradients by appropriate interpolation. The shape of these contours reflects the low overall correlation between the two pressure gradients and the symmetry about the longitudinal direction. The application of the lowest threshold to the data, however, reveals preferential directions, as was shown above, which suggests strong correlation between the pressure gradients during violent events.

7. Further discussion and conditional sampling

An attempt has been made to identify the vorticity flux signals, particularly the high- and low-amplitude portions of the signal, with physical phenomena associated with the bursting process in the near-wall region of the boundary layer.

Direct numerical simulations as well as experimental data have shown the existence of vortical structures in the near-wall region which carry vorticity directed in several predominant orientations. Theodorsen (1952), for instance, first postulated that the hairpin or horseshoe vortex is the dominant flow mechanism in turbulent boundary layers. Head & Bandyopadyay (1981) observed horseshoe vortices at low to relatively high Reynolds numbers inclined at 45° to the mean flow directions. Offen & Kline (1975) suggested the formation of either a spanwise vortex or an upward-tilted streamwise vortex as the key elements of the burst–sweep mechanism. Robinson's (1990) studies of direct numerical simulation of data have shown the existence of quasi-streamwise vortices and 'arch' type vortices in the inner region of the boundary layer. Falco (1983) associated all these features of streamwise vortices, hairpin vortices and streaky structures with the movement of ring-type vortices, called typical eddies and pocket wall-region disturbances. The present results demonstrated that there is a predominant orientation of the vorticity flux vector which appears to be about 45° to the longitudinal direction during mild or violent events.

At this point it should be emphasized that vorticity flux and pressure gradients, which appear directly in the Navier–Stokes equations, are local quantities, like vorticity, describing events at the measuring point although they are derived from pressure which is a quantity affected globally by contributions from every point of the flow field. In that respect vorticity flux can be used to infer local phenomena. As was mentioned in the introduction the present measurements of vorticity flux can be interpreted as vorticity changes through equations (9) and (10). If the fluid is initially irrotational then the change in vorticity represents the actual vorticity of the fluid element after the action of the wall as was originally suggested by Lighthill (see figure 2). However there is a possibility of an initially rotational fluid element or ball approaching the wall and then changing its vorticity by $\Delta\omega$. In this case the actual vorticity of the fluid element after the interaction with the wall is not known. However

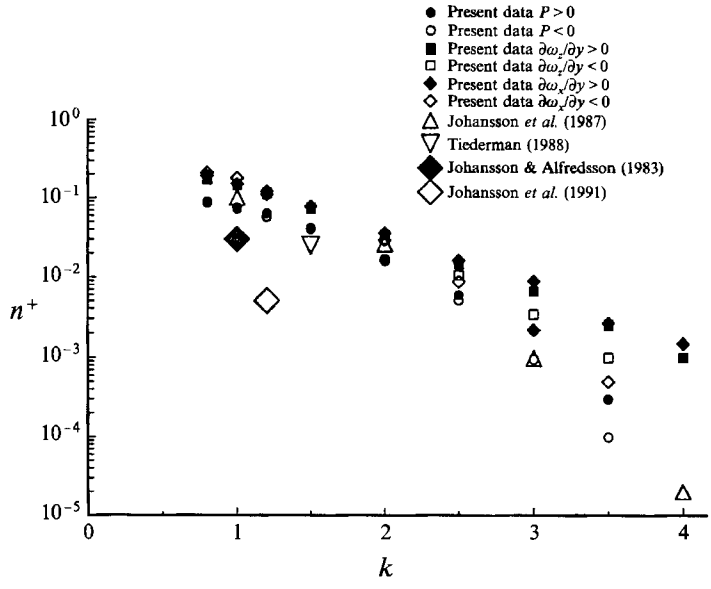

FIGURE 24. Bursting frequency dependence on threshold value k.

during very strong events vorticity changes may be substantially larger than the initial vorticity. This can be seen by comparing $\Delta\omega_z^+$ with a typical vorticity value like the mean vorticity at the wall $\overline{\omega_z^+} = -1$:

$$|\Delta\omega_z^+|/|\overline{\omega_z^+}| = k\left(\frac{\partial\omega^+}{\partial y^+}\right)_{r.m.s.}\Delta y^+.$$

For $k = 3$ and Δy^+ in the range between 10 and 100 the above ratio appears to be between 1.8 and 18. In that respect it may be possible to assume that during very strong events, which involve initially rotational flow elements, the change of vorticity may represent, to a good approximation, the actual vorticity itself. Under these assumptions, ejections which carry fluid of negative ω_z away from the wall (see Morrison, Subramanian & Bradshaw 1992) are expected to be characterized by positive $\partial\omega_z/\partial y$. Negative $\partial\omega_z/\partial y$ is expected to be the distinguishing feature of sweeps which are indicative of high-speed fluid moving towards the wall. Formation of horseshoe or arch type vortices in the near wall which carry negative ω_z vorticity requires events detected in the I and IV quadrants. If a mushroom vortex, which is itself an axisymmetric structure, is lifted up away from the wall, the distribution of p.d.f. of θ should be uniform across all four quadrants. However the present distribution, shown in figure 22, is far from uniform. This indicates that substantial asymmetries exists in the near-wall vortical structures. Falco's typical eddies, if these are perceived as the tips of the horseshoe vortices, after some substantial rotation may qualify as a typical candidate structure of this flow since they possess some of the characteristic features exhibited in the p.d.f. distribution of θ. However Falco (1993) attributes their origin to the outer layer rather than the wall and therefore the present results cannot be interpreted in terms of typical eddies.

To further explore the physics of these high-amplitude peaks of vorticity flux the previously mentioned conditional-sampling technique has been extended to detect the peak value of the signal during the time it is above the threshold value. Then all these

events are referenced to their peak value and ensemble averaged to obtain the 'typical' structure. Events corresponding to high-amplitude signals were detected for both positive and negative peaks of vorticity flux for various threshold levels.

Pressure peaks have been found to be strongly related to near-wall shear layers and vortices. Johansson *et al.* (1987), and Haritonidis *et al.* (1988) have shown that shear-layer structures (Willmarth & Sharma 1984) in the buffer region cause the large positive wall-pressure peaks. Johansson, Alfredsson & Kim (1991) who analysed the database generated from the direct numerical simulation of channel flows drew similar conclusions. It appears therefore that the strong coupling of positive pressure peaks and buffer-region shear layers is present in a variety of flows: low-Reynolds-number pipe flow, turbulent boundary layers and turbulent spots. Robinson (1990, 1991) has associated strong negative pressure peaks with the passage of near-wall vortices, while Johansson *et al.* attributed them to sweep-type motions.

Since these features of large pressure fluctuations are associated with specific physical phenomena the pressure signal can provide the necessary link between the educed vorticity flux patterns and physical events with known pressure signatures.

The significance of the detected flow structures and their dynamics depends strongly on their frequency of occurrence. The number of events detected with the present algorithm has been found to be a function of the threshold value of k. Figure 24 shows the detected events per unit time, n^+, scaled with inner variables, as a function of k, for the positive or negative $\partial\omega_x/\partial y$-peak events, the positive or negative $\partial\omega_z/\partial y$-peak events and positive or negative pressure-peak events. The present data based on pressure-peak detection compare rather well with the data of Johansson *et al.* (1987) obtained with a similar data processing technique. The data of Tiederman (1988), Luchik & Tiederman (1987) and Johansson & Alfredsson (1982), both based on the Variable Integral Time Average (VITA) technique of Blackwelder & Kaplan (1976) for detecting accelerated events in the buffer region, are also plotted for comparison, together with the results of Johansson *et al.* (1991) obtained from the direct numerical simulations of a rather low Reynolds number channel flow.

One distinguishing feature of the present results is the larger number of events detected by the vorticity-flux-peak technique than by the VITA or pressure-peak techniques. On average, n^+ obtained from the vorticity flux signal is about 60–90% higher than that obtained from the pressure signal. However, if one considers that the p.d.f. of vorticity flux has longer tails than the corresponding p.d.f. of pressure fluctuations, this behaviour is not a surprise: vorticity flux signals contain more high-amplitude fluctuations than pressure. These fluctuations are features of dynamically important events which cannot be easily depicted from the pressure or velocity signals.

Although n^+ is a rather strong function of the threshold level k, the flow patterns deduced by these techniques are much less dependent on threshold. It has been found in the past by Johansson & Alfredsson (1982) and Johansson *et al.* (1987) that the shape of the patterns obtained at various threshold level settings is, qualitatively, the same. In fact, Johansson *et al.* (1987) demonstrated that all patterns collapse when normalized with k. Figures 25(*a*), 25(*b*) and 25(*c*) show typical flow patterns of $\partial\omega_x/\partial y$, $\partial\omega_z/\partial$y and pressure obtained after conditioning on the positive $\partial\omega_x/\partial y$ and detected with different threshold levels $k = 1$, 2 and 3 respectively. The qualitative agreement among the three sets of results is fairly good. As the threshold increases stronger events contribute more to the ensemble-average pattern and therefore some of the features become more pronounced. For this reason only results obtained with $k = 3$ will be presented and discussed here.

Positive $\partial\omega_x/\partial y$ events correspond very closely to positive pressure events which are

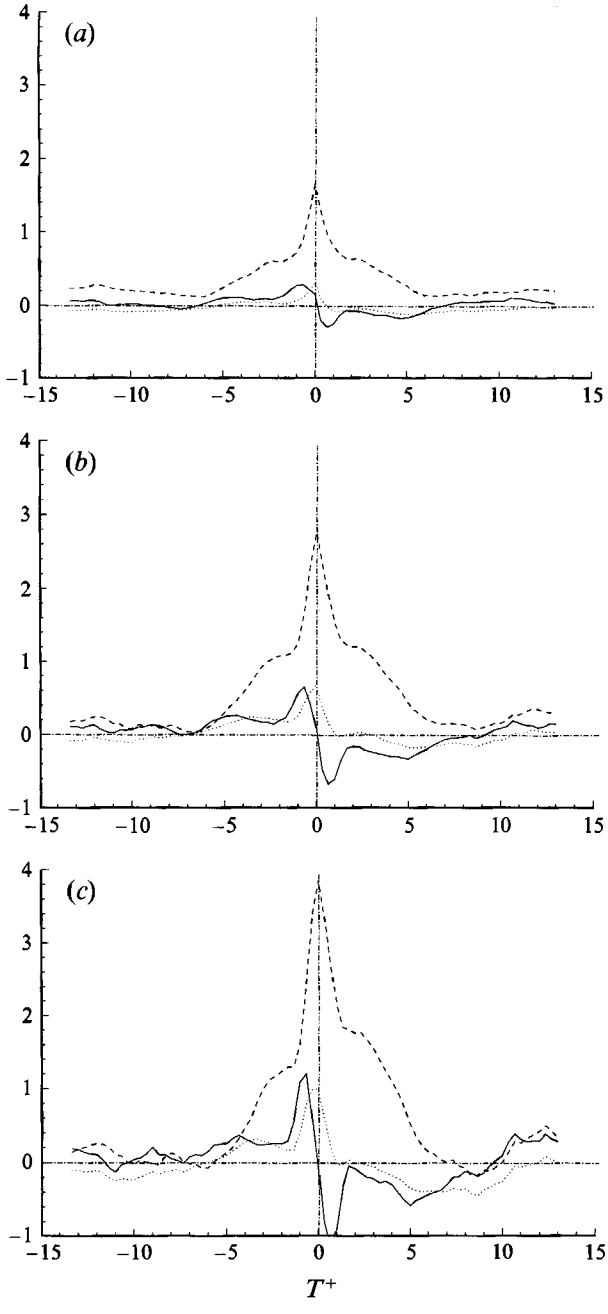

FIGURE 25. Conditionally averaged patterns based on $\partial\omega_x/\partial y > 0$: (*a*) $k = 1$, (*b*) $k = 2$, (*c*) $k = 3$. ....., Pressure; -.-.-.-, $\partial\omega_x/\partial y > 0$; ——, $\partial\omega_z/\partial y > 0$.

present during ejections and are associated with the shear layers. The main characteristic, however, of the patterns shown in figure 25(*c*) is the existence of peaks in the vorticity flux which may be directly attributed to the formation of vortices in the flow. This hypothesis is not unreasonable given the fact that these peaks are very narrow and sharp. Under these conditions the major feature of the vorticity flux appears to be the change of sign of $\partial\omega_z/\partial y$, occuring at $T^+ = 0$, which indicates the

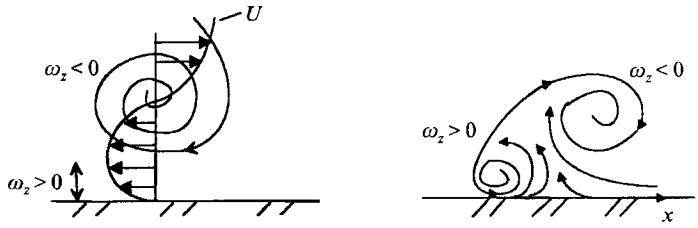

FIGURE 26. Conceptual wall structure.

existence of a secondary vortex of opposite sign. Since the present technique detects vorticity entering the flow from the wall, the patterns of figure 25(*c*) strongly suggest the formation or generation of a new vortex rather than the convection of an existing secondary vortex from downstream. The present data show that the formation of the primary vortex with positive $\partial\omega_z/\partial y$ is followed by the formation of a secondary vortex with negative $\partial\omega_z/\partial y$. A wave pattern preceding the formation of the vortices is also evident in the present data at negative T^+. This may indicate the existence of some local instability pattern of a near-wall vorticity layer with an apparent period of about 3 viscous time units.

The primary vortex, as a result of a strong interaction with the wall, induces a layer of secondary wall vorticity of opposite sign (see figure 26) which then separates and rolls up to form a vortex of opposite sign. This mechanism of flow separation induced by a vortex pair has been proposed by Ersoy & Walker (1986) who investigated numerically the interaction of two-dimensional vortex motion near a wall in an effort to understand the dynamics of the bursting phenomenon. Experimentally, the existence of counter-rotating vortices has been proposed by Blackwelder & Eckelman (1979) in the case of longitudinal vortices in the near-wall region. Orlandi & Jimenez (1991) have also shown the formation of a secondary longitudinal vortex in their numerical experiments of artificial wall flow. The $\partial\omega_x/\partial y$ pattern of figure 25(*c*) also shows a change of sign at $T^+ = 7.5$ indicating the formation of a counter-rotating pair of longitudinal vortices which, however, are a pair of the same vortical structure as the $\partial\omega_z/\partial y$ pattern. If the peaks in $\partial\omega_z/\partial y$ represent the core of the vortices then the timescale of the formation of the structure is about $T_V^+ = 2$. This rather short time is only a small fraction of the bursting cycle, which is considered to be of the order of 100. However, during this rapid evolution there is considerable interaction between the two vortices leading to large pressure fluctuations which are associated with the transfer of turbulent kinetic energy from the component normal to the wall to the other two and the generation of large wall shear stress. At this point it should be mentioned that Morrison *et al.* (1992) detected features in the ejections/sweeps similar to those of Falco's 'typical eddies' which they observed in the logarithmic region of a boundary layer over a smooth wall. Their ω_z-ensemble-averaged structure during sweeps is very similar to the $\partial\omega_z/\partial y$ pattern shown in figure 25(*c*). They also measured considerable overshoot of the local shear stress signal during the passage of the counter-rotating pairs of vortices.

Klewicki, Falco & Foss (1992) have measured the average duration time of positive or negative ω_z events as a function of Re_θ. For $Re_\theta = 2870$, which is very close to the present case of $Re_\theta = 3100$, a value of 2 is measured for each of these events which are characteristic of vortex-ring-like 'typical eddy' motions in the outer region of the boundary layer where corrugations in the turbulent/non-turbulent interface take place. The average duration of these events, which have a large timelife, is the same as

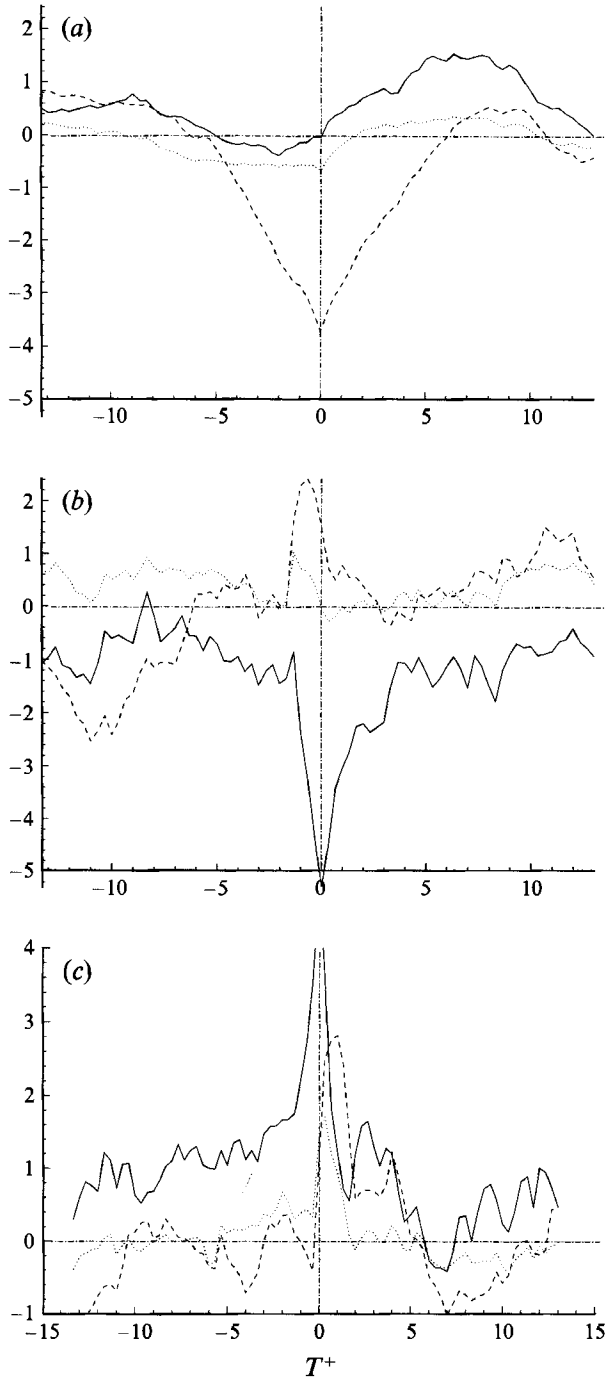

FIGURE 27. Conditionally averaged patterns based on (*a*) $\partial\omega_x/\partial y < 0$, $k = -3$; (*b*) $\partial\omega_z/\partial y < 0$, $k = -3$; (*c*) $\partial\omega_z/\partial y > 0$, $k = 3$. ·····, Pressure; -·-·-·-, $\partial\omega_x/\partial y$; ——, $\partial\omega_z/\partial y$.

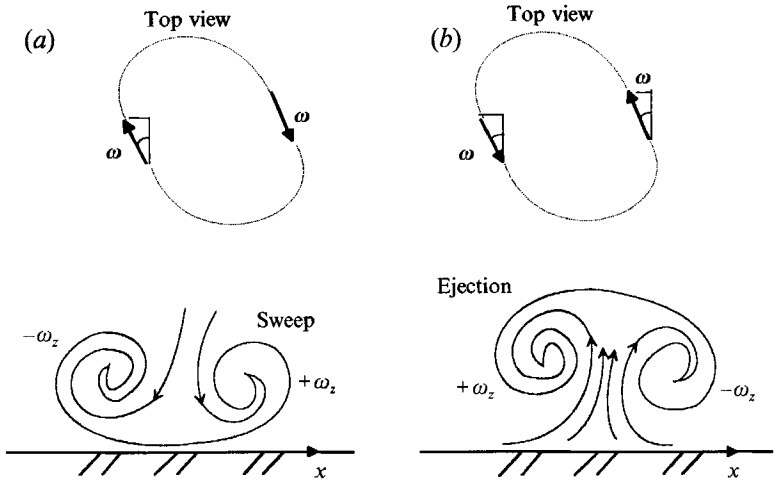

FIGURE 28. Conceptual structure of (*a*) sweeps, (*b*) ejections.

the formation time of the present $\partial\omega_z/\partial y$ events at the wall. This may suggest that these typical eddies are counter-rotating vortical structures which are originated at the wall and subsequently transported away from the wall with substantial change in their duration, although transformation from a counter-rotating pair to a single vortex may take place. There is however, a possibility that these structures are also formed somewhere inside the boundary layer and then dispersed throughout the flow field as has been claimed by Falco (1993). The fact that they have been observed in the present study to be formed at the wall during ejections and to pass through the logarithmic region again during ejections and sweeps (see Morrison *et al.* 1992) indicates that most probably they are originated at the wall, and that they constitute one of the principal mechanisms of communication and interaction between the inner and outer layers since they carry a significant amount of shear stress and kinetic energy.

A change in sign is also observed in the longitudinal vorticity flux at about $T^+ = 7.5$. This, however, leads to a rather weak vorticity flux pattern which cannot be characterized as a discrete secondary longitudinal vortex. In that respect the present results agree with Robinson's (1990) finding that occurrence of a counter-rotating pair of longitudinal vortices (legs) is rather rare at low Reynolds numbers. However, isolated longitudinal vortices carrying negative ω_x have been found in the present study. Figure 27(*a*) shows the flow patterns of the data conditioned on negative $\partial\omega_x/\partial y$. Pressure and $\partial\omega_z/\partial y$ closely follow the pattern of each other with some time lag. At $T^+ < -6.0$ $\partial\omega_z/\partial y$ is positive and then changes sign to become negative, indicating again the existence of counter-rotating vortices. However, at $T^+ > 0$ the spanwise component increases substantially. This type of configuration is consistent with the characteristics of symmetric arch-like vortices with one leg oriented entirely in the longitudinal direction.

More evidence for the existence of flow structures carrying mostly strong spanwise vorticity are shown in figures 27(*b*) and 27(*c*) where the $\partial\omega_z/\partial y$-conditioned results are plotted. Sweeps ($u > 0, v < 0$) are present just upstream of a vortex with dominant spanwise vorticity and are associated with $\partial p/\partial t < 0$ ($\partial p/\partial x > 0$) and ejections ($u < 0, v > 0$) are present just downstream ($T^+ < 0$) of these vortical structures where pressure increases with time ($\partial p/\partial x < 0$). As can be seen from figure 27(*b*) sweeps are mostly associated with negative vorticity flux $\partial\omega_z/\partial y$ and positive $\partial\omega_x/\partial y$. At the end

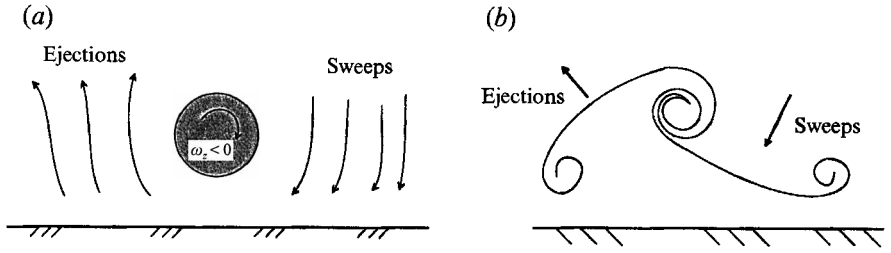

FIGURE 29. (*a*) Classical model of ejections and sweeps in reference to an arch type of vortex. (*b*) Conceptual model of combined ejections/sweeps.

of the sweeps $\partial\omega_z/\partial y$ has reached its largest negative value. It is apparent from the results that ejections (figure 27*c*) are generating considerable activities involving large longitudinal vorticity.

Sweeps, which are usually characterized as high-momentum outer-layer fluid moving towards the wall, can be considered as an impulse of a jet-like fluid motion splashing on the wall. Morrison *et al.* (1992) and Morrison & Bradshaw (1991) postulated that sweeps are inverted mushroom vortices moving towards the wall and then toppled by mean vorticity to form an ejection further downstream. The major implication of this model is that there are no arch-type or Λ-type vortices in the near wall and that the lobe of the mushroom vortex with negative ω_z accounts for what has been observed as arch-type or Λ-type vortices. The model indicates that these mushroom vortices are recycled during the bursting process without accounting for their origin. The present results, however, suggest that structures similar to distorted mushroom vortices are indeed formed at the wall as a result of some instability mechanism of the thin vorticity layer in the region next to the wall, and then they are ejected away from the wall, where they have a rather long life.

It should be noted that the results of the present conditioning refer to structures with either positive or negative peaks in $\partial\omega_z/\partial y$. A typical flow structure however may contain fluid carrying both peaks of vorticity flux, one positive and one negative. Sweeps, for instance, may be characterized by $\partial p/\partial t < 0$ with $\partial\omega_z/\partial y < 0$ as in figure 27(*b*) for $T^+ < 0$ and $\partial p/\partial t < 0$ with $\partial\omega_z/\partial y > 0$ as in figure 27(*c*) for $T^+ > 0$. Figure 28(*a*) depicts a candidate structure for the strong-vorticity-flux events with one positive ω_z approaching the wall.

Similarly, events with $\partial p/\partial t > 0$ may be associated with a structure like that of figure 28(*b*) which carries fluid with positive and negative ω_z away from the wall. This type of structure is identified with derivatives in the longitudinal direction $\partial\omega_z/\partial x < 0$ while that of figure 28(*a*) is characterized by $\partial\omega_z/\partial x > 0$.

Thus the typical flow structure at the wall consists of sweeps and ejections which are associated with both negative and positive spanwise vorticity ω_z and positive and negative longitudinal vorticity ω_x. This flow structure should be compared with the classical view of sweeps and ejections which can be found downstream and upstream respectively of a strong arch-type vortex with negative ω_z (see figure 29*a*). If the flow structure of figures 28(*a*) and 28(*b*) has to comply with the classical view, the two lobes of the mushroom vortices of figure 28(*a*, *b*) which carry negative vorticity have to coincide and the typical eddy structure may look like what is shown in figure 29(*b*).

However, there is one more possible scenario which is also in accord with the present conclusions and is closer to the classical view of a strong vortex with negative ω_z which brings down to the wall fluid upstream of this vortex. This fluid splashes on the wall like a jet impinging on a solid surface and the upstream-moving fluid creates a vorticity

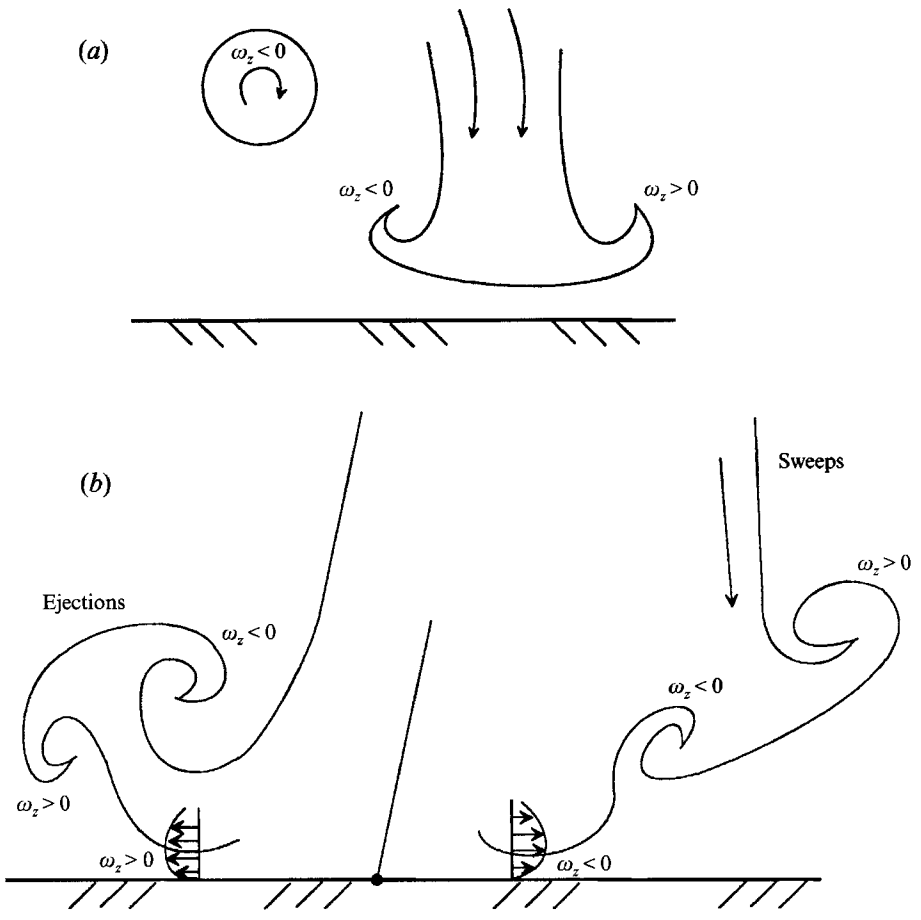

FIGURE 30. (*a*) Conceptual model of inrushing fluid as a jet impinging on the wall. (*b*) Conceptual mechanism of ejections and sweep formation.

layer with positive ω_z which then rolls up into a vortex moving away from the wall. Meanwhile the upstream-moving fluid forms a vorticity layer with negative ω_z which also separates and rolls up into a vortex. Figures 30(*a*) and 30(*b*) depict this scenario.

8. Conclusions

An attempt has been made to measure time-dependent vorticity flux density at the wall beneath a two-dimensional zero-pressure-gradient, turbulent boundary layer. Since the net viscous force on an incompressible fluid element is dominated by the local gradients of vorticity the understanding of their features is the key to determining the turbulence structure. The concept of vorticity flux was first introduced by Lighthill (1963) who pointed out the significance of solid boundaries as distributed sources or sinks of vorticity. It indicates the amount of vorticity entering the flow, which cannot be obtained from considering vorticity at the wall. Lighthill also suggested a mechanism explaining how a local pressure gradient tangential to the boundary can cause an initially irrotational fluid element to roll up along a stationary wall and acquire vorticity due to the non-slip condition at the wall.

Four high-frequency-response and high-sensitivity subminiature pressure transducers were used to measure time-dependent pressure gradients simultaneously.

Statistics of the pressure fluctuations, as measured individually by each of these transducers, agree rather well with previous results reported by other investigators. This established a certain degree of reliability of the probe for vorticity flux measurements. The present analysis indicated that the major contributions to vorticity flux come from the uncorrelated part of the two pressure signals which contain a wide range of eddy size scales from large to small eddies. Large scales may also contribute to vorticity flux. Two pressure signals, for instance in the form of sine waves with the same frequency, are perfectly correlated and produce zero vorticity flux. However, if a small phase difference exists between them then the correlation drops to a value below 1.0 and a non-zero vorticity flux is produced. Although large scales contribute to vorticity flux, small scales seem to contribute relatively more because the degree of correlation among small scales is considerably lower. This imposes a severe requirement on the spatial resolution of the vorticity flux probe. Extension of the theories of Corcos (1963) and Wilmarth & Roos (1965) on the resolution of pressure measurements to include cases of pressure gradient measurements predicted a larger attenuation of vorticity flux than of pressure for all eddy scales which are smaller than the transducer size. It is believed that the present measurements, although probably not entirely immune from the problem of spatial resolution, have captured most of the energy of fluctuating pressure and vorticity flux in the high-frequency range of the spectra. In particular, the spatial resolution in the low-Re case is one of the best ever achieved.

The results indicated a rather strong dependence of all vorticity flux statistics on Re_θ when plotted in inner wall scales. Scaling the data with θ and u_τ substantially reduced the Reynolds number dependence and indicated an outer-layer influence on the wall.

The distribution of the probability density function reveal the presence of extremely high and low amplitudes of both vorticity gradients which contribute substantially to the statistics although their probability of appearance is rather low. It appears that the mechanism by which a fluid element acquires vorticity at the wall is a rather violent event with high amplitude of $\partial\omega_x/\partial y$ and $\partial\omega_z/\partial y$ followed by periods of small-amplitude fluctuations.

The transport equations derived for the vorticity flux, σ, show that the mechanism of vortex stretching or compression which is present in the vorticity transport equation is also present here. This indicates possible similarities in the description of physical mechanisms by both vorticity and vorticity flux.

The results of the conditional-sampling analysis indicate that a very significant small-scale turbulent structure is present when large contributions to vorticity flux occur. The patterns obtained show that during strong events opposite vorticity is present immediately after the primary vortex appears. The data suggest that the primary vortex induces a layer of secondary wall vorticity of opposite sign which rolls up to form a vortex of opposite sign. Thus the major wall structure appears to be bipolar, most likely in the form of mushroom vortices. This is also supported by the orientation of the vorticity flux vector. In addition, ejections and sweeps are associated with this structure: during ejections fluid in the form of a bipolar vortex is leaving the wall violently while during sweeps a similar structure impinges on the wall. Thus the structure of ejections and sweeps appears to be more complicated than simple violent outgoing or inrushing fluid in the near-wall region.

The financial support of the National Science Foundation is greatly acknowledged. Dr A. Honkan's assistance in the acquisition of some of the data is appreciated. The authors are grateful to the referees for their comments and suggestions.

Appendix

Following Uberoi & Kovasznay (1954) and Corcos (1963), for a homogeneous and stationary turbulent flow, the measured pressure p_m sensed by a transducer of diameter $2r$ with instantaneous time response can be derived from the true pressure field through the following relation:

$$p_m(\boldsymbol{x}, t) = \int_\infty p(\boldsymbol{s})\, K(\boldsymbol{s}-\boldsymbol{x})\, \mathrm{d}A(\boldsymbol{s}), \tag{A 1}$$

where $\boldsymbol{x}$ is the position vector, $K(\boldsymbol{s}-\boldsymbol{x})$ is the response kernel, i.e. the contribution to the output signal at time t which is caused by unit pressure at location $\boldsymbol{s}$. It is also assumed that $K(\boldsymbol{s}) = 1/\sigma$ whenever $\boldsymbol{s}$ corresponds to a point on the transducer face and $K(\boldsymbol{s}) = 0$ otherwise. Here σ is the sensing area of the transducer and $\boldsymbol{i}$ is the unit vector in the x-direction.

If the measured spanwise vorticity flux is defined as

$$\omega_m(\boldsymbol{x}, t) = \frac{p_m(\boldsymbol{x}+2r\boldsymbol{i}, t) - p_m(\boldsymbol{x}, t)}{2r}, \tag{A 2}$$

where $2r$ is the diameter of each transducer, then substituting (A 1) into (A 2) gives

$$\omega_m(\boldsymbol{x}, t) = \frac{1}{2r}\left\{\int_\infty p(\boldsymbol{s}, t)\, K(\boldsymbol{s}-\boldsymbol{x}-2r\boldsymbol{i})\, \mathrm{d}A(\boldsymbol{s}) - \int_\infty p(\boldsymbol{s}, t)\, K(\boldsymbol{s}-\boldsymbol{x})\, \mathrm{d}A(\boldsymbol{s})\right\}. \tag{A 3}$$

The measured frequency spectrum is given by

$$\phi_m(\omega_f) = \frac{1}{2\pi}\int_\infty R_m(0, \tau)\, \mathrm{e}^{-\mathrm{i}\omega_f \tau}\, \mathrm{d}\tau, \tag{A 4}$$

where ω_f is the frequency and R_m is the cross-correlation defined for vorticity flux as

$$R_{\omega_m}(\boldsymbol{\zeta}, \tau) = \langle \omega_m(\boldsymbol{x}, t)\, \omega_m(\boldsymbol{x}+\boldsymbol{\zeta}, t+\tau)\rangle. \tag{A 5}$$

If $\omega_m(\boldsymbol{x}, t)$ and $\omega_m(\boldsymbol{x}+\boldsymbol{\zeta}, t+\tau)$ are substituted by (A 3), then after some manipulation the following relation can be obtained:

$$\begin{aligned} R_{\omega_m}(\boldsymbol{\zeta}, \tau) = \frac{1}{4r^2}\Bigg\{ & \iint_\infty R_p(\boldsymbol{\eta}+\boldsymbol{\zeta}-\boldsymbol{s}, \tau)\, K(\boldsymbol{s})\, K(\boldsymbol{\eta})\, \mathrm{d}A(\boldsymbol{s})\, \mathrm{d}A(\boldsymbol{\eta}) \\ & - \iint_\infty R_p(\boldsymbol{\eta}+\boldsymbol{\zeta}+2r\boldsymbol{i}-\boldsymbol{s}, \tau)\, K(\boldsymbol{s})\, K(\boldsymbol{\eta})\, \mathrm{d}A(\boldsymbol{s})\, \mathrm{d}A(\boldsymbol{\eta}) \\ & - \iint_\infty R_p(\boldsymbol{\eta}+\boldsymbol{\zeta}-2r\boldsymbol{i}-\boldsymbol{s}, \tau)\, K(\boldsymbol{s})\, K(\boldsymbol{\eta})\, \mathrm{d}A(\boldsymbol{s})\, \mathrm{d}A(\boldsymbol{\eta}) \\ & + \iint_\infty R_p(\boldsymbol{\eta}+\boldsymbol{\zeta}-\boldsymbol{s}, \tau)\, K(\boldsymbol{s})\, K(\boldsymbol{\eta})\, \mathrm{d}A(\boldsymbol{s})\, \mathrm{d}A(\boldsymbol{\eta})\Bigg\}, \end{aligned} \tag{A 6}$$

where R_p is the cross-correlation of the true pressure field and $\mathrm{d}A$ is the area element at points $\boldsymbol{s}$ and $\boldsymbol{\eta}$. Then the frequency spectra ϕ_{ω_m} will take the form

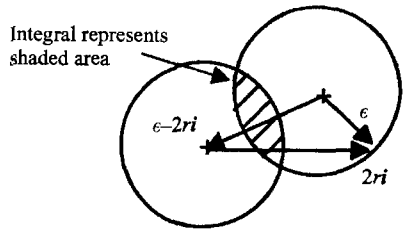

FIGURE 31. Graphical representation of $\theta(\epsilon)$.

$$\phi_{\omega_m}(\omega_f) = \Big\{\iint_\infty \Gamma_p(\boldsymbol{\eta}-\boldsymbol{s},\omega_f)\,K(\boldsymbol{s})\,K(\boldsymbol{\eta})\,\mathrm{d}A(\boldsymbol{s})\,\mathrm{d}A(\boldsymbol{\eta}) - \iint_\infty \Gamma_p(\boldsymbol{\eta}+2r\boldsymbol{i}-\boldsymbol{s},\omega_f)\,K(\boldsymbol{s})\,K(\boldsymbol{\eta})\,\mathrm{d}A(\boldsymbol{s})\,\mathrm{d}A(\boldsymbol{\eta}) - \iint_\infty \Gamma_p(\boldsymbol{\eta}-2r\boldsymbol{i}-\boldsymbol{s},\omega_f)\,K(\boldsymbol{s})\,K(\boldsymbol{\eta})\,\mathrm{d}A(\boldsymbol{s})\,\mathrm{d}A(\boldsymbol{\eta}) + \iint_\infty \Gamma_p(\boldsymbol{\eta}-\boldsymbol{s},\omega_f)\,K(\boldsymbol{s})\,K(\boldsymbol{\eta})\,\mathrm{d}A(\boldsymbol{s})\,\mathrm{d}A(\boldsymbol{\eta})\Big\}, \tag{A 7}$$

where Γ is the cross-spectral density given by

$$\Gamma(\boldsymbol{\gamma},\omega_f) = \frac{1}{2\pi}\int^\infty R(\boldsymbol{\gamma},\tau)\,\mathrm{e}^{-\mathrm{i}\omega_f\tau}\,\mathrm{d}\tau. \tag{A 8}$$

This term has been modelled by Corcos (1963) and Willmarth & Roos (1965) as

$$\Gamma(\xi,\eta,\omega_f) = \phi_p(\omega_f)\,A\left(\frac{\omega_f\xi}{U_c}\right)B\left(\frac{\omega_f\eta}{U_c}\right)\mathrm{e}^{\omega_f\xi/U_c}, \tag{A 9}$$

where A and B are cross-spectral similarity solutions of the parameters $\omega_f\xi/U_c$ and $\omega_f\eta/U_c$ respectively and η and ξ are the components of the distance vector $\boldsymbol{\gamma}$. ϕ_p is the true frequency spectrum of pressure.

These functional relations are also supported by experimental evidence. Their analytical expressions and numerical values are found in Corcos (1963) and Willmarth & Roos (1965). Then the previous expression for ϕ_{ω_m} is rewritten using (A 9) as

$$\frac{\phi_{\omega_m}(\omega_f)}{\phi_p(\omega_f)} = \frac{1}{8\pi r^2}\Big\{2\int_\infty \theta(\epsilon)\,A\left(\frac{\omega_f\epsilon_x}{U_c}\right)B\left(\frac{\omega_f\epsilon_y}{U_c}\right)\mathrm{e}^{-\mathrm{i}\omega_f\epsilon_x/U_c}\,\mathrm{d}A(\boldsymbol{\varepsilon}) - \int\theta(\epsilon+2r\boldsymbol{i})\,A\left(\frac{\omega_f\epsilon_x}{U_c}\right)B\left(\frac{\omega_f\epsilon_y}{U_c}\right)\mathrm{e}^{-\mathrm{i}\omega_f\epsilon_x/U_c}\,\mathrm{d}A(\boldsymbol{\varepsilon}) - \int\theta(\epsilon-2r\boldsymbol{i})\,A\left(\frac{\omega_f\epsilon_x}{U_c}\right)B\left(\frac{\omega_f\epsilon_y}{U_c}\right)\mathrm{e}^{-\mathrm{i}\omega_f\epsilon_x/U_c}\,\mathrm{d}A(\boldsymbol{\varepsilon})\Big\}, \tag{A 10}$$

where ϵ_x and ϵ_y are the components of $\boldsymbol{\varepsilon}$, and $\theta(\boldsymbol{\varepsilon})$ is Corcos' correlation function given by

$$\theta(\epsilon) = \int_\infty K(\boldsymbol{s})\,K(\boldsymbol{s}+\epsilon)\,\mathrm{d}A(\boldsymbol{s}). \tag{A 11}$$

Similarly,

$$\theta(\epsilon-2r\boldsymbol{i}) = \int_\infty K(\boldsymbol{s})\,K(\boldsymbol{s}+\epsilon-2r\boldsymbol{i})\,\mathrm{d}A(\boldsymbol{s}). \tag{A 12}$$

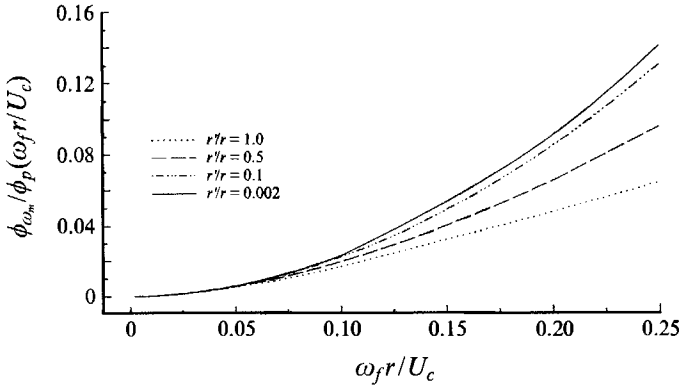

FIGURE 32. Ratio of spectrum of vorticity flux and true spectrum of pressure as a function of $\omega_f r/U_c$.

The latter function is represented pictorially in figure 31 as the area intersected by two transducer surfaces at a distance $\epsilon - 2ri$ from each other. And $\theta(\epsilon + 2ri)$ can be represented in a similar fashion.

Since there is no previous information about the true frequency spectrum of vorticity flux, $\phi_\omega(\omega_f)$, a best estimate has been obtained from equation (A 10) in the limit of r approaching zero. Figure 32 depicts values of ϕ_{ω_m}/ϕ_p obtained as a function of $\omega r/U_c$. This figure clearly shows the rate of convergence of the above ratio as a function of the relative transducer size.

Similar estimates can be obtained for the other vorticity flux component $\partial p/\partial z = \rho\nu\,\partial\omega_x/\partial y$.

REFERENCES

ALFREDSSON, P. H. & JOHANSSON, A. V. 1984 Time scales in turbulent channel flow. *Phys. Fluids* **27**, 1974.

ANDREOPOULOS, J., DURST, F. & JOVANOVIC, J. 1984 Influence of Reynolds number on characteristics of turbulent boundary layers. *Exps. Fluids* **2**, 7.

ASHURST, W. T., KERSTEIN, A. R., KERR, R. M. & GIBSON, C. H. 1987 Alignment of vorticity and scalar gradient with strain rate in simulated Navier–Stokes turbulence. *Phys. Fluids* **30**, 2343.

BALINT, J. L., WALLACE, J. M. & VUKOSLAVCEVIC, P. 1991 Vorticity and velocity fields of a turbulent boundary layer. *J. Fluid Mech.* **228**, 53.

BRADSHAW, P. 1967 Inactive motion and pressure fluctuations in turbulent boundary layers. *J. Fluid Mech.* **30**, 241.

BLACKWELDER, R. F. & ECKELMAN, H. 1979 Streamwise vortices associated with the bursting phenomenon. *J. Fluid Mech.* **94**, 577.

BLACKWELDER, R. F. & KAPLAN, R. E. 1976 On the bursting phenomenon near the wall in bounded turbulent shear flows. *J. Fluid Mech.* **76**, 89.

BLAKE, W. K. 1970 Turbulent boundary-layer wall-pressure fluctuations on smooth and rough walls. *J. Fluid Mech.* **44**, 637.

BULL, M. K. 1967 Wall pressure fluctuations associated with subsonic turbulent boundary layer flow. *J. Fluid Mech.* **28**, 719.

COLES, D. E. 1962 The turbulent boundary layer in a compressible fluid. In *Rand Rep.* R403-PR., ARC 24473: *Appendix A: A Manual of Experimental Boundary Layer Practice for Low Speed Flow.*

CORCOS, G. M. 1963 On the resolution of pressure in turbulence. *J. Acoust. Soc. Am.* **35**, 192.

DEVENPORT, W. J., AGARWAL, N. K., DEWITZ, M. B., SIMPSON, R. L. & PODDAR, K. 1990 Effects of a fillet on the flow past a wing-body junction. *AIAA J.* **28**, 2017.

ERSOY, S. & WALKER, J. D. A. 1986 Flow induced at a wall by a vortex pair. *AIAA J.* **24**, 1597.

FALCO, R. E. 1983 New results. A review and synthesis of the mechanism of turbulent production in boundary layers and its modification. *AIAA Paper* 83-0377.

FALCO, R. E. 1993 Predictions of the Reynolds number dependence of the turbulent boundary layer using a new structural model. *Symposium on Near Wall Turbulence* (ed. R. So, C. Speziale & B. Launder). Elsevier.

FARABEE, T. M. & CASARELLA, M. J. 1991 Spectral features of wall pressure fluctuations beneath a turbulent boundary layer. *Phys. Fluids* A **3**, 2410.

GAD-EL-HAK, M. & BANDYOPANDYAY, P. R. 1994 Reynolds number effects in wall-bounded turbulent flows. *Appl. Mech. Rev.* **47**, 307.

HANRATTY, T. J. 1988 A conceptual model of the viscous wall region. *Zoran Zaric Memorial Conference* (ed. S. Kline & N. Afgan), p. 81. Hemisphere.

HARITONIDIS, J. H., GRESCKO, L. S. & BREUER, K. S. 1988 Wall pressure peaks and spectra. *Zoran Zaric Memorial Conference* (ed. S. Kline & N. Afgan), p. 397. Hemisphere.

HASAN, M. A. Z., CASARELLA, M. J. & ROOD, E. D. 1986 An experimental study of the wall pressure field around a wing-body junction. *Trans. ASME J. Vib., Acoustics, Stress and Reliability in Design* **108**, 308.

HEAD, M. R. & BANDYOPADHYAY, P. 1981 New aspects of turbulent boundary layer structure. *J. Fluid Mech.* **107**, 297.

HONKAN, A. 1994 An experimental study of the vortical structure of turbulent flows. PhD thesis, Dept. of Mech. Engng, City College of CUNY.

JIMENEZ, J. & MOIN, P. 1991 The minimal flow unit in near-wall turbulence. *J. Fluid Mech.* **225**, 213.

JOHANSSON, A. V. & ALFREDSSON, P. H. 1982 On the structure of turbulent channel flow. *J. Fluid Mech.* **122**, 295.

JOHANSSON, A. V., ALFREDSSON, P. H. & KIM, J. 1991 Evolution and dynamics of shear-layer structures in near-wall turbulence. *J. Fluid Mech.* **224**, 579.

JOHANSSON, A. V., HER, J.-Y. & HARITONIDIS, J. H. 1987 On the generation of high-amplitude wall pressure peaks in turbulent boundary layers and spots. *J. Fluid Mech.* **175**, 119.

KEITH, W. L., HURDIS, D. A. & ABRAHAM, B. M. 1992 A comparison of turbulent boundary layer wall-pressure spectra. *Trans. ASME J. Fluids Engng* **114**, 338.

KIM, J. 1989 On the structure of pressure fluctuations in simulated turbulent channel flows. *J. Fluid Mech.* **205**, 421.

KIM, H. T., KLINE, S. J. & REYNOLDS, W. C. 1971 The production of turbulence near a smooth wall in a turbulent boundary layer. *J. Fluid Mech.* **50**, 133.

KIM, J. & MOIN, P. 1986 The structure of the vorticity field in turbulent channel flow. Part 2. Study of ensemble-average fields. *J. Fluid Mech.* **162**, 339.

KLEWICKI, J. C. & FALCO, R. E. 1990 On accurately measuring statistics associated with small-scale structure in turbulent boundary layers using hot-wire probes. *J. Fluid Mech.* **219**, 119.

KLEWICKI, J. C., FALCO, R. E. & FOSS, J. F. 1992 Some characteristics of the vortical motions in the outer region of turbulent boundary layers. *Trans. ASME J. Fluids Engng* **114**, 530.

KLINE, S. J., REYNOLDS, W. C., SCHRAUB, F. A. & RUNSTADLER, P. W. 1967 The structure of turbulent boundary layers. *J. Fluid Mech.* **30**, 741.

LIGHTHILL, M. J. 1963 Boundary layer theory. In *Laminar Boundary Layers* (ed. L. Rosenhead), p. 46. Oxford University Press.

LU, L. J. & SMITH, C. R. 1988 Image processing of hydrogen bubble flow visualization for quantitative evaluation of hairpin type vortices as a flow structure of turbulent boundary layers. *Rep.* FM-14. Lehigh University.

LUCHIK, T. S. & TIEDERMAN, W. G. 1987 Timescale and structure of injections and bursts in turbulent channel flows. *J. Fluid Mech.* **174**, 529.

LYMAN, F. A. 1990 Vorticity production at a solid boundary. *Appl. Mech. Rev.* **43**, 157.

MCGRATH, B. E. & SIMPSON, R. L. 1987 Some features of pressure fluctuations in turbulent boundary layers with zero and favorable pressure gradient. *NASA Rep.* CR-4051.

MOIN, P. & KIM, J. 1985 The structure of vorticity fields in turbulent channel flow. Part 1. Analysis of instantaneous field and statistical correlations. *J. Fluid Mech.* **155**, 441.

MORRISON, J. F. & BRADSHAW, P. 1991 Bursts and sources of pressure fluctuation in turbulent boundary layers. *Eighth Symp. on Turbulent Shear Flows, Tech. University of Munich.*

MORRISON, J. F., SREENIVASAN, C. S. & BRADSHAW, P. 1992 Bursts and the law of the wall in turbulent boundary layers. *J. Fluid Mech.* **241**, 75.

NAGUIB, A. M. & WARK, C. K. 1992 An investigation of wall-layer dynamics using a combined temporal filtering and correlation technique. *J. Fluid Mech.* **243**, 541.

OFFEN, G. R. & KLINE, S. J. 1975 A proposed model of the bursting process in turbulent boundary layers. *J. Fluid Mech.* **70**, 209.

ORLANDI, P. & JIMENEZ, J. 1991 A model for bursting of near wall vortical structures in boundary layers. *Eighth Symp. on Turbulent Shear Flows, Tech. University of Munich.*

PANTON, R. L. 1984 *Incompressible Flows.* Wiley Interscience.

PANTON, R. L. & GILLES, R. 1992 The turbulent boundary layer pressure spectrum. *Bull. Am. Phys. Soc.* **37**, 1702.

ROBINSON, S. K. 1990 A perspective on coherent structures and conceptual models for turbulent boundary layer physics. *AIAA 21st Fluid Dynamics, Plasmadynamics and Lasers Conf.*, Seattle *WA*, *Paper* 90-1638.

ROBINSON, S. K. 1991 Coherent motions in the turbulent boundary layer. *Ann. Rev. Fluid Mech.* **23**, 601.

SCHEWE, G. 1983 On the structure and resolution of wall-pressure fluctuations associated with turbulent boundary layer flow. *J. Fluid Mech.* **134**, 311.

SHAH, D. A. & ANTONIA, R. A. 1989 Scaling of the bursting period in turbulent boundary layer and duct flows. *Phys. Fluids* A **1**, 318.

SPALART, P. R. 1988 Direct numerical simulation of a turbulent boundary layer up to $Re = 1410$. *J. Fluid Mech.* **187**, 61.

THEODORSEN, T. 1952 Mechanism of turbulence. In *Proc. 2nd Midwestern Conf. on Fluid Mechanics, Ohio State University*, p. 1.

THOMAS, A. S. W. & BULL, M. K. 1983 On the role of wall-pressure fluctuations in deterministic motions in the turbulent boundary layer. *J. Fluid Mech.* **128**, 283.

TIEDERMAN, W. G. 1988 Eulerian detection of turbulent bursts. *Zoran Zaric Memorial Conference* (ed. S. Kline & N. Afgan), p. 874. Hemisphere.

UBEROI, M. A. & KOVASZNAY, L. S. G. 1953 On the mapping of random signals. *Q. Appl. Maths* **10**, 375.

WILLMARTH, W. W. 1975 Pressure fluctuations beneath turbulent boundary layers. *Ann. Rev. Fluid Mech.* **7**, 13.

WILLMARTH, W. W. & ROOS, F. W. 1965 Resolution and structure of the wall pressure field beneath a turbulent boundary layer. *J. Fluid Mech.* **22**, 81.

WILLMARTH, W. W. & SHARMA, L. K. 1984 Study of turbulent structure with hot wires smaller than the viscous length. *J. Fluid Mech.* **142**, 121.

WILLMARTH, W. W. & WOOLDRIDGE, C. E. 1962 Measurements of the fluctuating pressure at the wall beneath a thick turbulent boundary layer. *J. Fluid Mech.* **14**, 187.